

II. PLASMA DYNAMICS

A. PLASMA PHYSICS*

Prof. S. C. Brown
 Prof. W. P. Allis
 Prof. D. J. Rose
 Prof. D. R. Whitehouse
 Dr. G. Bekefi
 Dr. B. Brandt
 Dr. Magda Ericson

Dr. S. Gruber
 Dr. J. L. Hirshfield
 D. E. Baldwin
 C. D. Buntschuh
 J. D. Coccoli
 E. W. Fitzgerald
 S. Frankenthal

P. J. Freyheit
 R. B. Hall
 W. R. Kittredge
 J. J. McCarthy
 W. J. Mulligan
 J. J. Nolan, Jr.
 Judith S. Vaughen

1. ELECTRON TEMPERATURE AND DENSITY VARIATIONS IN A SPATIALLY DECAYING PLASMA

In Quarterly Progress Reports No. 56 (pages 21-25) and No. 57 (pages 5-7) we considered the axial (z) variation of electron density n and energy U of a cylindrical plasma column in an axial magnetic field, produced at $z = 0$ and allowed to diffuse to the region $z > 0$. It was found that in the limit of free-electron diffusion, $n(z)$ and $U(z)$ are the solutions of the following equations:

$$nU = (nU)_0 J_0(2.4r/R) \exp(-\beta z) \quad (1)$$

$$\frac{d^2 U}{dz_0^2} - 2 \frac{dU}{dz_0} = \gamma \left(1 - \frac{1}{U}\right) \quad (2)$$

where $\beta = (2.4/R) \left(1 + \mu_-^2 B^2\right)^{-1/2}$, $\gamma = 9Gv_-^2/10 U_e \beta^2$, $\underline{U} = U/U_e$, and $z_0 = \beta z$. However, in the previous reports it was erroneously assumed that the transition from free to ambipolar diffusion can be made by merely replacing β by $\beta_a = (2.4/R) \left(1 + \mu_+ \mu_- B^2\right)^{-1/2}$. We present here the correct result that is applicable in the presence of ambipolar diffusion, subject to the assumption that $\mu_- \gg \mu_+$.

The Boltzmann equation gives for the heat flux \vec{H} carried by the electrons,

$$\vec{H} = \frac{5}{3} U \vec{\Gamma} - \frac{10}{9} \frac{nU}{m} \vec{\tau} \cdot \vec{\nabla} U \quad (3)$$

where $\vec{\Gamma}$ is the electron flow resulting from diffusion and space-charge fields. The rest of the notation is the same as that used previously. When the equations for the conservation of energy and charge are used to eliminate \vec{H} and $\vec{\Gamma}$ from Eq. 3, we obtain

$$nU = (nU)_0 J_0(2.4r/R) \exp(-\beta_a z) \quad (4)$$

* This work was supported in part by the Atomic Energy Commission under Contract AT(30-1)-1842; and in part by the Air Force Cambridge Research Center under Contract AF-19(604)-5992; and in part by National Science Foundation under Grant G-9330.

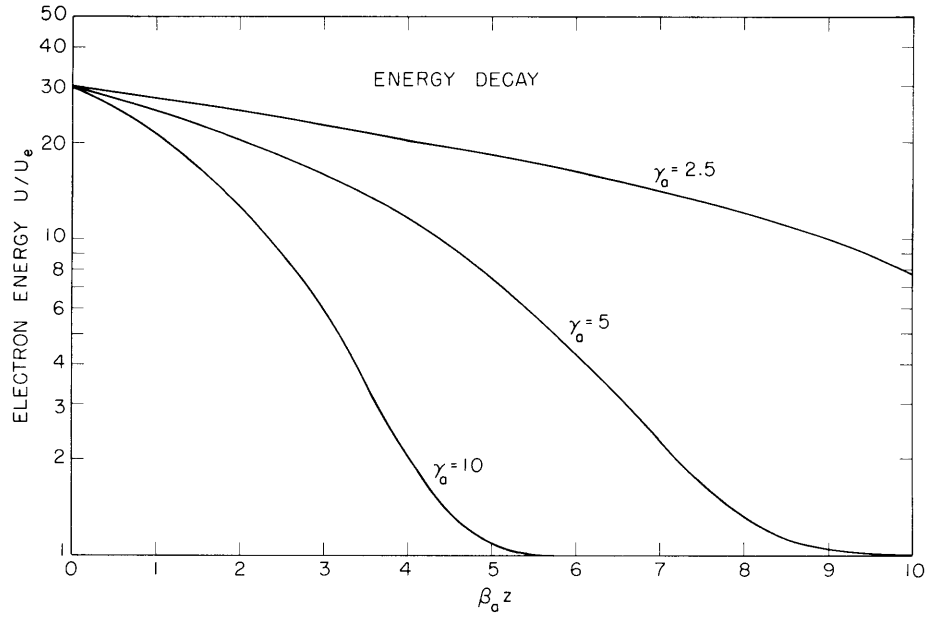


Fig. II-1. Electron energy as function of distance from the active discharge.

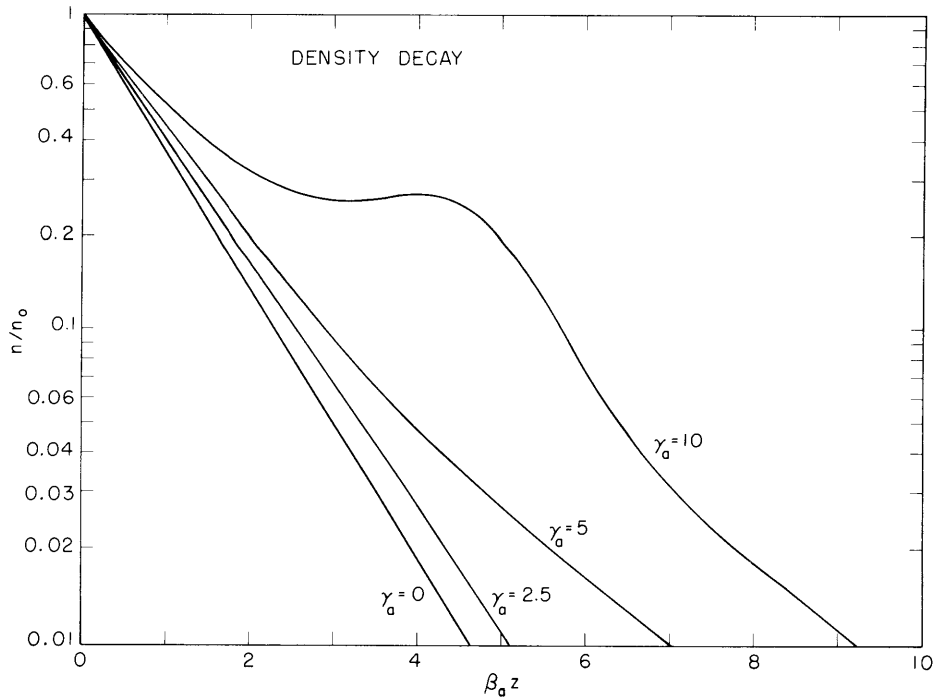


Fig. II-2. Electron density as function of distance from the active discharge.

and

$$\frac{d^2 \underline{U}}{dz_o^2} - \frac{d \underline{U}}{dz_o} = \gamma_a \left(1 - \frac{1}{\underline{U}} \right) \quad (5)$$

where $z_o = \beta_a z$ and $\gamma_a = 9Gv_-^2/10 U_e \beta_a^2$. Equations 4 and 5 for ambipolar diffusion are equivalent to Eqs. 1 and 2 for free diffusion.

Figures II-1 and II-2 show how U and n vary with $\beta_a z$ for several values of the constant γ_a . Note in Fig. II-2 that when $\gamma_a = 10$ the electron density does not fall off monotonically. The reasons for this have been discussed in the earlier reports. It can be shown that this local increase in n can only occur when $\gamma \geq 12$, and when $\gamma_a \geq 8$. From these limits we can compute the minimum magnetic field for which such an electron increase could occur. For a helium plasma of 1-cm radius that has decayed almost to room temperature U_e , the ambipolar limit gives a minimum magnetic field of approximately 2000 gauss.

G. Bekefi, D. R. Whitehouse

2. MICROWAVE MEASUREMENTS OF PLASMA TEMPERATURES

In Quarterly Progress Report No. 57 (pages 7-11) we described an instrument for measuring the radiation temperature T of a plasma. Here, we summarize the results of the measurements that were made with this pyrometer on the positive columns of dc discharges in helium, neon, and hydrogen.

The discharge tube had a 1.25-cm radius, R , and was 100 cm long. It was inserted in the broad face of an S-band waveguide at an angle of 8° with respect to the waveguide axis. In this manner, a section of the positive column, 50 cm long, was situated inside the waveguide. Lengths of brass tubing, 3.5 inches long, attached to the waveguide, surrounded the plasma column that protruded from the waveguide. The brass tubing acted as a waveguide beyond cutoff, and thus prevented the radiation generated at the electrodes from entering the measuring region. Since at high electron densities the chokes can become ineffective (as a result of coaxial waveguide propagation), microwave absorbing material was wrapped around the remaining part of the discharge tube.

Figure II-3 shows the variation of T in helium as a function of the gas pressure p_o , normalized to 0°C . The measurements were made for three different discharge currents. The theoretical curve, obtained from von Engel and Steenbeck (1), represents the electron temperature. At certain pressures (see for instance, the curve in Fig. II-3 for 0.1 amp and $p_o R \sim 0.9$) gaps will be noted in the measurements. In these regions, the temperature changed violently by as much as a factor of 2. These variations are not yet understood. Their presence or absence, and their magnitude depend, to some

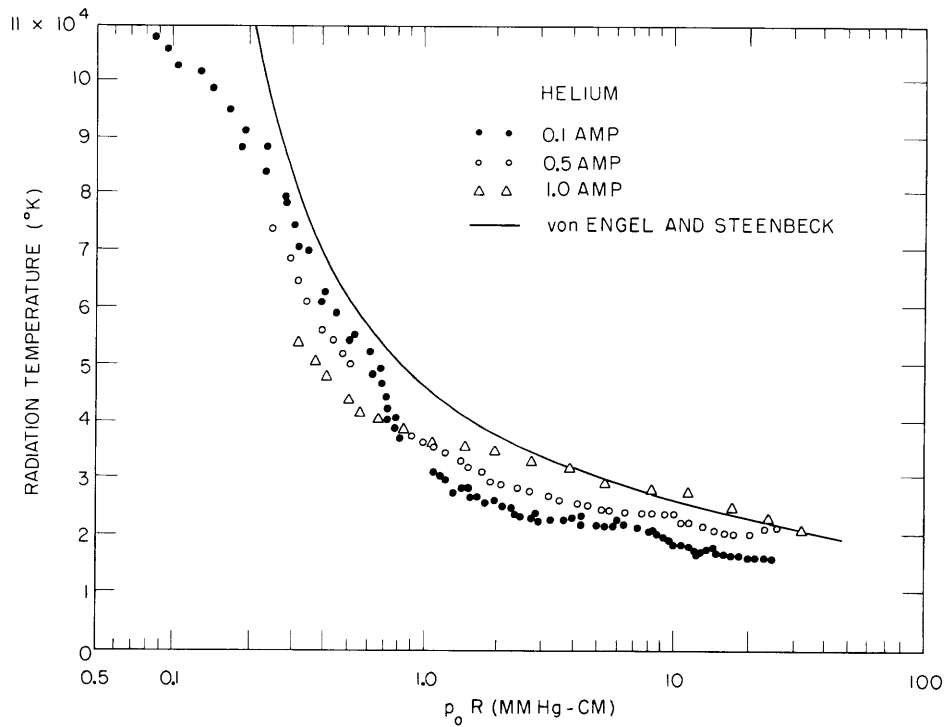


Fig. II-3. Radiation temperature as a function of gas pressure for three discharge currents in helium.

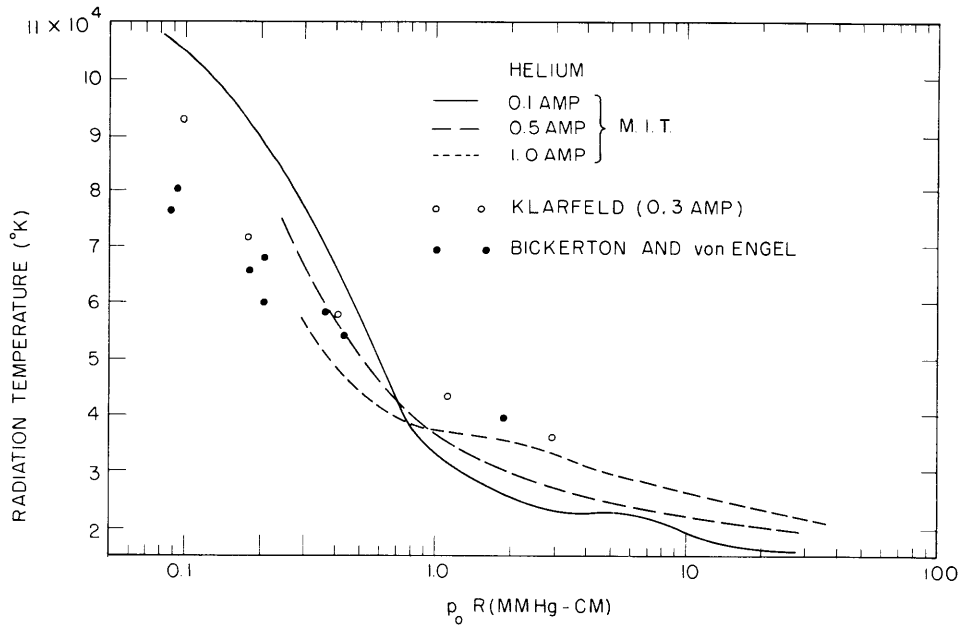


Fig. II-4. Comparison of radiation measurements of temperature (lines) with Langmuir probe measurements (circles and points) in helium.

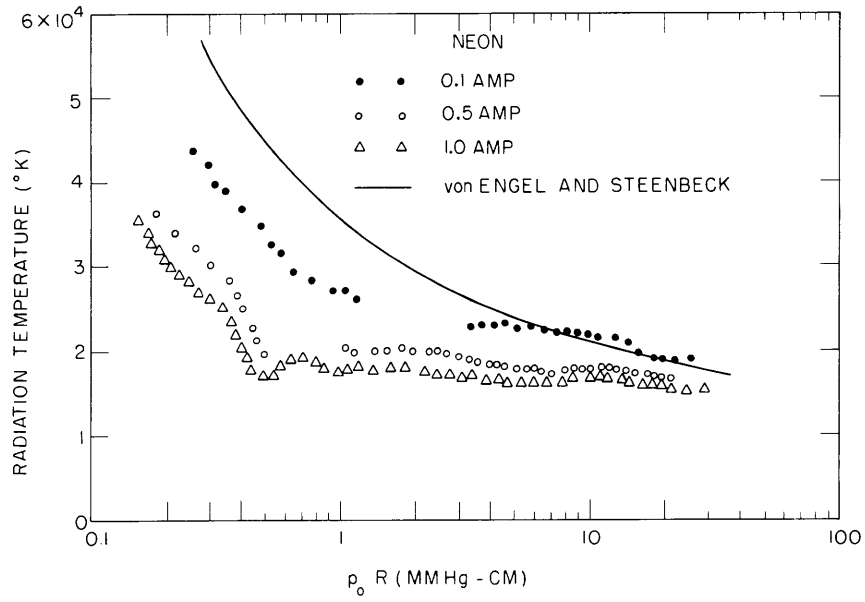


Fig. II-5. Temperature as a function of pressure in neon.

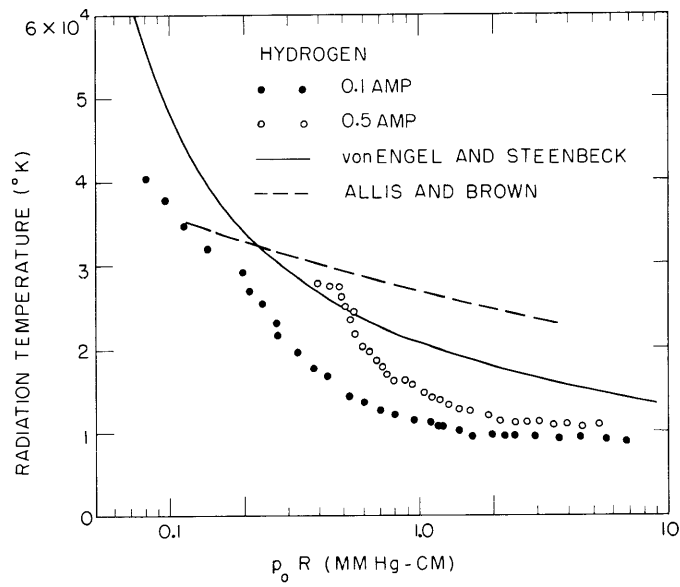


Fig. II-6. Temperature as a function of pressure in hydrogen.

(II. PLASMA DYNAMICS)

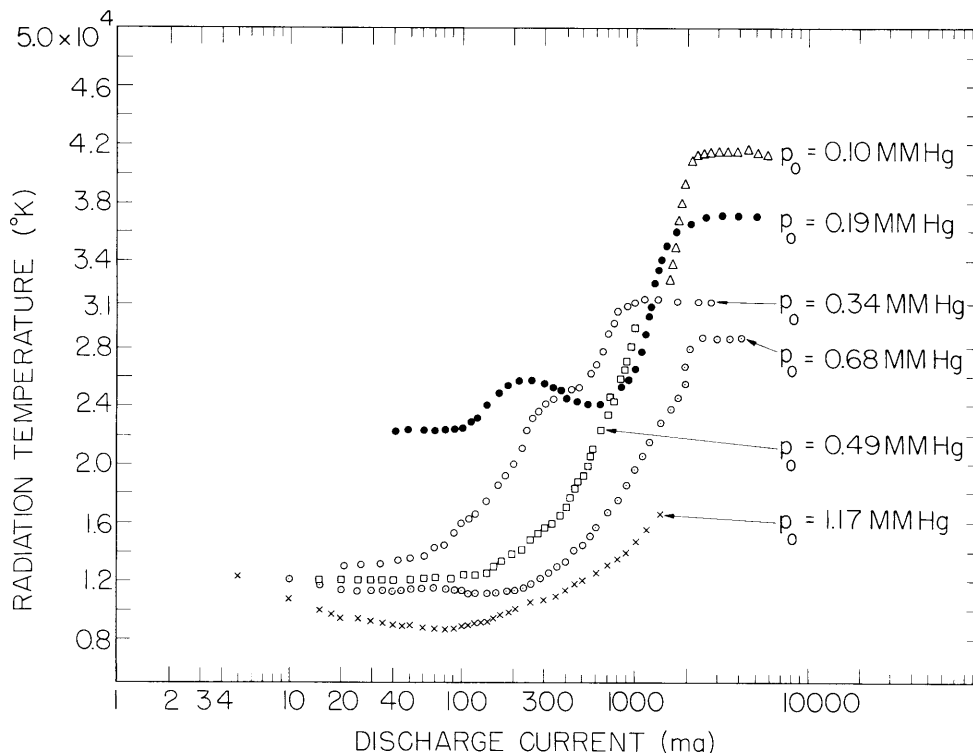


Fig. II-7. Temperature as a function of discharge current for various pressures in hydrogen.

extent, on the size of the resistance in series with the discharge, but more strongly on the heating current through the oxide-coated cathode. All readings found to be sensitive to the cathode current were discarded as not being representative of the "normal" quiescent operation of the positive column.

Figure II-4 shows the measurements depicted in Fig. II-3 compared with probe measurements of the electron temperature (2, 3). Figure II-5 presents measurements for neon, and Fig. II-6, those for hydrogen. For hydrogen measurements, we also show the results of computations of the electron energy made by Allis and Brown (4), who derived the energy as a function of p_0/E , where E is the axial electric field. Having measured E in our discharges, we could then evaluate the variation of T with p_0 . The calculations of Allis and Brown were made by equating the energy gained by an electron with the energy lost by excitation, ionization, and recoil with gas molecules. These calculations show poor agreement with von Engel and Steenbeck's less rigorous calculations made by equating the rate of creation of particles by ionization with the rate of loss by ambipolar diffusion. We feel that this disagreement is due partly to Allis and Brown's neglect of electron loss that is generally ascribed to excitation of vibration and rotation of the molecule.

Figure II-7 shows how T in hydrogen varies with the discharge current for various

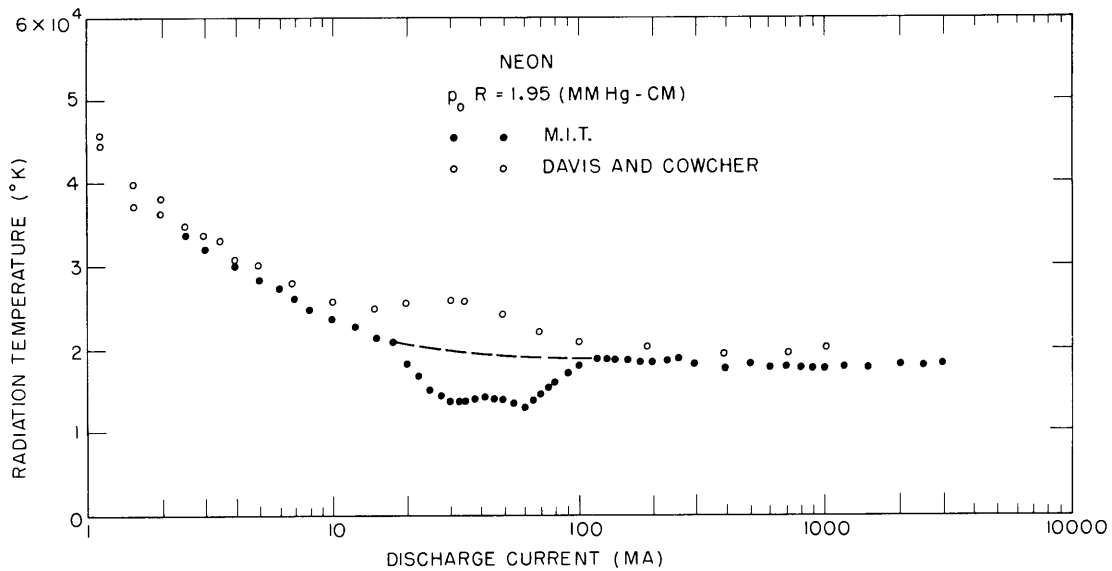


Fig. II-8. Temperature as a function of current in neon.

gas pressures. These measurements were motivated by the interesting work of Dreicer (5), who studied theoretically the effect on the electron energy as the degree of ionization in the plasma is increased. In a hydrogen discharge of our geometry, the ratio of electron density n to molecule density N is given by

$$\frac{n}{N} \approx 2.7 \times 10^{-5} \frac{I}{V}$$

where I is the discharge current in milliamperes, and V the voltage across the positive column, in volts. In all of our measurements, V ranged between 300 and 1200 volts, so that the degree of ionization and I are related by

$$\frac{n}{N} \approx 4 \times 10^{-8} I$$

We find that in our range of measurements ($10^{-7} \leq n/N \leq 3 \times 10^{-4}$) the agreement with Dreicer's calculations is only qualitative.

Figure II-8 shows how our measurements of the radiation temperature T agree with those obtained with a completely different technique by Davis and Cowcher (6). The agreement is very good except in the region shown by the dashed line. In this region, we observed the aforementioned cathode-dependent effects, and Davis and Cowcher concluded that probably the radiation here is partly nonthermal in character.

G. Bekefi

(References on following page)

(II. PLASMA DYNAMICS)

References

1. A. von Engel and M. Steenbeck, *Electrische gasentladungen, ihre Physik und Technik*, Vol. 2 (Springer Verlag, Berlin, 1932), p. 86.
2. B. Klarfeld, *Technical Physics of the U. S. S. R.*, Vol. 5, p. 725, 1938.
3. R. J. Bickerton and A. von Engel, *Proc. Phys. Soc. (London)* 69B, 468 (1956).
4. W. P. Allis and S. C. Brown, *Phys. Rev.* 87, 419 (1952).
5. H. Dreicer, *Phys. Rev.* 117, 343 (1960).
6. L. W. Davis and E. Cowcher, *Australian J. Phys.* 8, 108 (1955).

3. RECEIVING-ANTENNA INFLUENCE ON CYCLOTRON RADIATION MEASUREMENTS

The measured shape of a pressure-broadened cyclotron radiation line is modified by the length of time spent by an average electron within the region of observation. This effect becomes important at low gas pressures when the probability of an electron making a collision within the region of observation is small. The line shape is then determined by the time spent crossing the receiving-antenna aperture, and by the antenna pattern at the plasma under observation.

With reference to Fig. II-9, the n^{th} electron radiates a field, E_n , where $E_n \sim \cos(\omega_b t + \phi_n)$. The phase angle, ϕ_n , is included to take into account the interparticle phase relationship. The field received, E_{rn} , is weighted by the antenna pattern, so that

$$E_{rn} \sim \cos(\omega_b t + \phi_n) g[v_n(t - \xi_n)] \tag{1}$$

Here, we introduce ξ_n as the time when the n^{th} particle arrives at $x = 0$, the center of the pattern.

We must now find the power measured by the receiver at the radian frequency, ω , which results from all of the electrons with velocities between v and $v + dv$, $f(v) dv$, and then sum over all possible velocities (neglecting relativistic mass change). Here

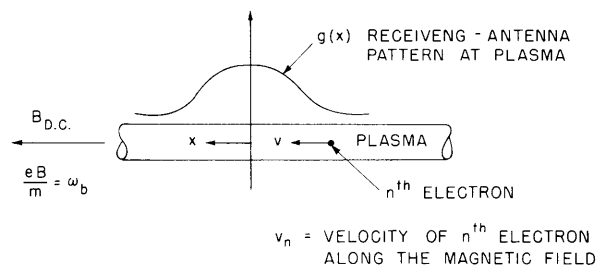


Fig. II-9. Geometry for the measurements.

$f(v)$ is the one-dimensional velocity distribution.

The power density spectrum is given by

$$P(\omega) \sim \int_{-\infty}^{\infty} \left\{ \left| G\left(\frac{\omega - \omega_b}{v}\right) \right|^2 + \left| G\left(\frac{\omega + \omega_b}{v}\right) \right|^2 \right\} \frac{f(v)}{v} dv \quad (2)$$

where

$$G(K) = \int_{-\infty}^{\infty} g(x) e^{-jKx} dx \quad (3)$$

The assumptions inherent in Eq. 2 are that the electron does not make a collision that causes loss of coherence, and that the dc magnetic field is uniform. In practical cases the spatial function $g(x)$ has a limited extent. If this function is important only over a dimension d , then the first assumption implies essentially that the mean-free path is large compared with d . The second assumption is justified only for those velocities satisfying the inequality

$$v > \frac{ed^2}{2\pi m} \nabla B$$

This inequality is obtained by considering the frequency modulation of the cyclotron radiation as small, but it may also be looked upon as a restriction that the broadening caused by the time of flight through the region of observation be greater than the change in cyclotron frequency.

We can find a function, $g(x)$, with the property that the power density spectrum gives the one-dimensional velocity distribution directly. An impulse for $G(K)$, and hence a sinusoid for $g(x)$, gives this one-to-one relationship. Hence,

$$P(\omega) \sim \frac{f(v)}{v} \Big|_{v = (\omega - \omega_b)/2\pi d} + \frac{f(v)}{v} \Big|_{v = (\omega + \omega_b)/2\pi d}$$

where d is the wavelength of the receiving-antenna pattern at the plasma. This situation is illustrated by Fig. II-10.

Illumination of the plasma, in this manner, may be realized by an interferometer arrangement. For example, one may use two dipole antennas at a distance D apart, and at distance L from the plasma. The spatial period of the function $g(x)$ is given by

$$d = \frac{\lambda}{D} L = \frac{2\pi cL}{\omega_b D}$$

The collision frequency must be such that

(II. PLASMA DYNAMICS)

$$\frac{v}{v_c} > \frac{2\pi cL}{\omega_B D}$$

$$\frac{v_c}{\omega_B} < \frac{L}{2\pi D} \times \left(\frac{v}{c}\right)$$

Note that since $L \gg D$, this inequality is a less stringent requirement than the observation of Doppler shift for the determination of velocity distribution. However, sensitivity may be a problem in the first case.

An experiment is being carried out to observe this "transit-time" broadening of the

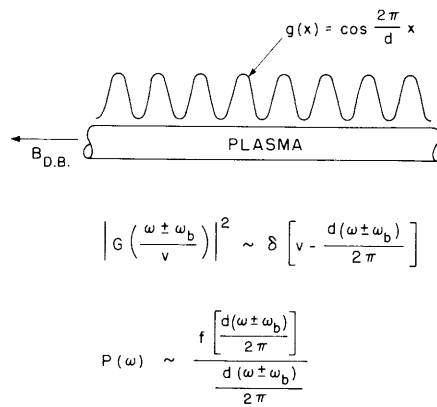


Fig. II-10. Receiving-antenna pattern for 1:1 relationship between power density spectrum and velocity distribution.

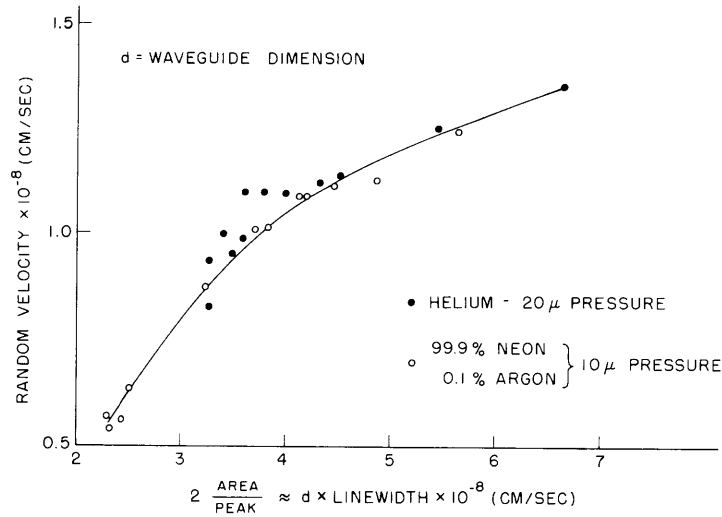


Fig. II-11. Transit-time broadening measurements.

cyclotron radiation at 8.2 kmc. The plasma is produced by a Penning Ion Gauge (pig) discharge between the poles of an electromagnet, and the cyclotron radiation is observed through an open X-band waveguide that touches a tube into which the plasma diffuses from the pig discharge. The electron density is sufficiently small that the single-particle picture given above applies. The potential of a collector at the end of this section of the discharge tube is varied from 0 to approximately 1500 volts positive with respect to the cathode, and electron current can be drawn. This affects both the temperature of the electrons and their directed velocity. By measuring the electron density with a TM_{010} cavity and then sweeping the dc magnetic field through the cyclotron line, we can find the electron temperature from the area under the line and also from the density (within some constant of proportionality given by the fraction of the radiation picked up by the open waveguide). The area of the curve divided by its peak amplitude is proportional to an effective width of the line. Data taken in this manner illustrate the effect. The points at the lower left of Fig. II-11 below the abscissa value of 3.5 were taken when no current was being drawn at the collector. The points in the upper right were obtained when current was drawn. The curve indicates that when no current is drawn the width of the line is proportional to the rms random velocity, whereas when current is drawn the proportionality is less, as would be expected when the effect of the directed velocity dominates the transit time.

S. Gruber

4. LINE PROFILES OF CYCLOTRON RADIATION

In Quarterly Progress Report No. 54 (pages 26-31), we demonstrated how equivalent theoretical descriptions of cyclotron radiation could be obtained, either from a single-particle model or from Kirchhoff's radiation law, by using the known absorption coefficients for waves in a plasma in a magnetic field. These theoretical results, together with their experimental substantiation, are applicable to plasmas whose collision frequency ν_c for electrons with heavy species is independent of electron velocity, and when the thermal motion of the electron does not influence the absorption of the waves.

In this report we extend the theory to cover both limitations and compare experimental results with the theory. As a side issue, we shall discuss a method of electron-temperature measurement that for low-temperature plasmas is independent of ν_c and of the spatial distribution of electron density, and we shall illustrate it with the results of typical measurements. Furthermore, we cite measurements of the Doppler shift of cyclotron radiation as a determination of electron-drift velocities in plasmas and discuss their limitations.

(II. PLASMA DYNAMICS)

a. Profile for Arbitrary $v_c(v)$ and No Thermal Effect

The cyclotron emission $dj(v, \omega)$ into a unit solid angle in a direction making an angle θ with the magnetic field, with the assumption of collision broadening to determine the spectrum (1), is given by

$$dj(v, \omega) dv d\omega = \frac{ne^2}{16\pi^2 \epsilon_0 c^3} v_{\perp}^2 \omega^2 \frac{v_c d\omega}{\pi} \frac{1}{(\omega - \omega_b)^2 + v_c^2} \left(\frac{1 + \cos^2 \theta}{2} \right) f(v) dv$$

where $nf(v) dv$ is the number of electrons in the velocity interval dv , and v_{\perp} is their component of velocity perpendicular to the applied magnetic field. For a Maxwellian velocity distribution, we sum over dv to obtain

$$j(\omega) d\omega = \left(\frac{m}{2\pi kT} \right)^{3/2} \frac{m\omega_p^2 \omega^2}{8\pi^2 c^3} \left(\frac{1 + \cos^2 \theta}{2} \right) \int_0^{\infty} \frac{v_c (d\omega/2\pi)}{(\omega - \omega_b)^2 + v_c^2} \exp\{-mv^2/2kT\} dv$$

In polar coordinates, $v_{\perp} = v \sin \theta$, and $d^3v = 2\pi v^2 \sin \theta d\theta dv$; hence we obtain

$$j(\omega) d\omega = \left(\frac{m}{2\pi kT} \right)^{3/2} \frac{m\omega_p^2 \omega^2}{3\pi c^3} \left(\frac{1 + \cos^2 \theta}{2} \right) \int_0^{\infty} \frac{v_c (d\omega/2\pi)}{(\omega - \omega_b)^2 + v_c^2} v^4 \exp\{-mv^2/2kT\} dv \quad (1)$$

As a complementary approach, we may proceed from the absorption coefficient $a(\omega)$ for the extraordinary wave propagating in a plasma at an angle θ with respect to the magnetic field, in the limit $(\omega_p^2/\omega_b v_c) \ll 1$.

$$a(\omega) = \left(\frac{m}{2\pi kT} \right)^{3/2} \frac{\omega_p^2}{c} \left(\frac{1 + \cos^2 \theta}{2} \right) \int_0^{\infty} \exp\{-mv^2/2kT\} \frac{d}{dv} \left[\frac{v_c}{v_c^2 + (\omega - \omega_b)^2} \frac{4\pi v^3}{3} \right] dv$$

Integrating by parts, we have

$$a(\omega) = \left(\frac{m}{2\pi kT} \right)^{3/2} \frac{4\pi}{3} \frac{m\omega_p^2}{kT} \left(\frac{1 + \cos^2 \theta}{2} \right) \int_0^{\infty} \frac{v_c}{v_c^2 + (\omega - \omega_b)^2} v^4 \exp\{-mv^2/2kT\} dv \quad (2)$$

Thus, from Eqs. 1 and 2, the ratio of emission to absorption is $kT\omega^2 d\omega/8\pi^3 c^2$ – the Rayleigh-Jeans intensity – and is independent of whatever dependence v_c may have on electron velocity v .

As an example, consider the case of constant collision probability P_c . The emission spectrum, from Eqs. 1 or 2 is then proportional to $\int_0^{\infty} \frac{x^2 e^{-x} dx}{x+a}$, where

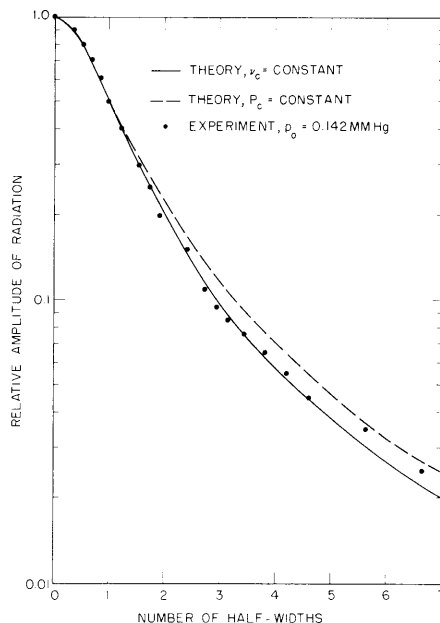


Fig. II-12. Profiles of cyclotron resonance radiation.

$$a = \frac{m}{2kT} \left(\frac{\omega - \omega_b}{pP_c} \right)^2$$
 for $\nu_c = pP_c\nu$, and $x = mv^2/2kT$. This integral has been tabulated (2) and is plotted in Fig. II-12, as the dashed line. The half-width is $(\omega - \omega_b)_{1/2} = 7.50 \times 10^5 pP_c (T_V)^{1/2}$, where T_V is the electron temperature in electron-volts. For comparison, the profile for constant ν_c , a Lorentz profile, is shown as the full curve. The difference between these two cases is relatively small; the P_c case is only 12 per cent higher than the ν_c case at five half-widths. Typical experimental values, obtained from a recorder trace of the profile, are shown as points. These data were obtained at 3000 mc with a Dicke radiometer, and by sweeping the magnetic field. The only difference between this experiment and earlier ones is that now the plasma, the positive column of a dc glow discharge in helium, is mounted along the axis of an S-band waveguide that is offset to allow the electrodes of the discharge tube to be outside the waveguide. The length of the plasma in the waveguide is 23 cm. A long plasma is chosen so that the transit-time effects, discussed by Gruber in Section II-A3, would be negligible and so that the polarization of the waves that interact with the plasma would not be strongly influenced by end effects. The experiment follows the ν_c case more closely but does not clearly distinguish either case because of the small differences.

b. Profiles Including Thermal Effects

We compute the absorption coefficient from the elements of the dielectric permittivity tensor \vec{K} , as given by Sitenko and Stepanov (3), introducing collisions by changing

(II. PLASMA DYNAMICS)

their ω to $\omega + i\nu_c$. Here, we consider only a wave propagating along the magnetic field.

$$\begin{aligned} a &= \frac{\epsilon}{c} \text{Im} (K_{11} + K_{12}) \\ &= \frac{\epsilon}{c} \text{Im} \left[\frac{\omega_p^2}{\omega} \frac{1}{\sqrt{\pi} k v_t} \int_{-\infty}^{\infty} \frac{e^{-y^2} dy}{\left(\frac{\omega - \omega_b + i\nu_c}{k v_t} \right) - y} \right] \end{aligned}$$

where the propagation constant k is assumed to have only a small imaginary part and to have a real part that differs negligibly from ω/c , that is, $k = k_0(1+i\gamma)$, with $\gamma \ll 1$, and where $v_t = \left(\frac{2kT}{m} \right)^{1/2}$. Under this assumption, we obtain

$$a = \gamma k_0 = \frac{\omega_p^2}{(\pi \omega v_t)^{1/2}} \int_{-\infty}^{\infty} \frac{(\beta - \gamma y)}{(\Omega - y)^2 + (\beta - \gamma y)^2} e^{-y^2} dy$$

where $\Omega = \frac{c}{v_t} \left(\frac{\omega - \omega_b}{\omega} \right)$, and $\beta = \frac{c}{v_t} \frac{\nu_c}{\omega}$. The denominator of the integral is approximately equal to $(\Omega - y)^2 + \beta^2$, provided that $\gamma \Omega \ll \beta$. With this same restriction, the numerator of the integral can be approximated as β alone. The restriction $\frac{\gamma \Omega}{\beta} \ll 1$ is equal approximately to

$$\frac{\gamma \Omega}{\beta} = \frac{c}{\omega} \frac{\omega_p^2 \Omega}{\omega_b v_t} \int_{-\infty}^{\infty} \frac{e^{-y^2} dy}{(\Omega - y)^2 + \beta^2} \approx \frac{c}{\omega} \frac{\omega_p^2}{\omega_b v_t} \frac{\Omega e^{-\Omega^2}}{\beta} \leq \frac{\omega_p^2}{\omega_b v_c}$$

which is exactly the restriction when the thermal effects are neglected. This is to ensure that the imaginary part of the index of refraction is small, so that the real part is approximately unity, and that the electrons may be considered as radiating into a vacuum. Thus, using Kirchhoff's law, we find that the result for the emission when both pressure broadening and thermal broadening (Doppler effect) occur, is proportional to

$$\int_{-\infty}^{\infty} \frac{e^{-y^2} dy}{(\Omega - y)^2 + \beta^2} \quad (3)$$

This is recognized as a Voigt profile (4), commonly used in spectroscopy when pressure broadening and Doppler broadening occur simultaneously.

Comparison of experimentally determined profiles with this theory is made in Fig. II-13. The curves for $\beta = \infty$ from Fig. II-12 are reproduced in order to emphasize the large differences between the Voigt profiles and the Lorentz profiles. For

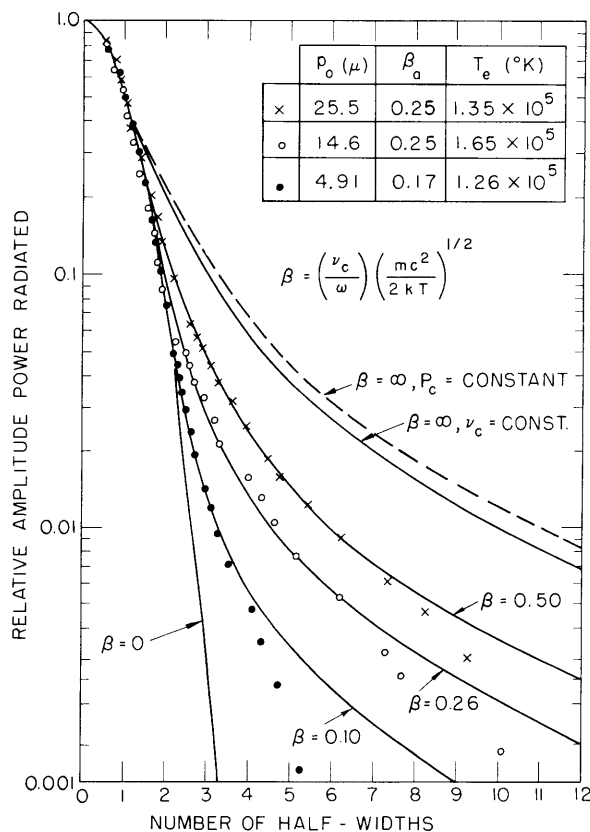


Fig. II-13. Profiles of cyclotron resonance radiation.

$\beta = 0$, the profile is approximately two orders of magnitude lower than that for $\beta = \infty$, at three half-widths. The inset in Fig. II-13 shows the values of pressure for which the experiments were obtained and values of electron temperature inferred from obtaining the best fit for experiment and theory.

Of significance is the experimental deviation from theory below a relative amplitude of 0.01. It is suggested that this could be due to a depletion in the tail of the electron-velocity distribution as compared with a Maxwellian, which is the distribution implicit in the theory. The parameter β_a listed in the inset of Fig. II-13 will be discussed below.

c. Effects of Opacity on Line Profile

Use of Eqs. 1, 2, or 3 to describe line profiles is, as we have seen, limited to cases in which $(\omega_p^2/\omega_b \nu_c) \ll 1$, and so the imaginary part of the index of refraction ($\alpha\lambda/4\pi$) is small compared with unity. However, for a plasma of size L , the radiation that is actually observed is proportional to $1 - e^{-\alpha L}$, from geometrical optics, if boundary reflections are neglected. In the experiment carried out here, $4\pi L/\lambda \approx 29$, so that αL

(II. PLASMA DYNAMICS)

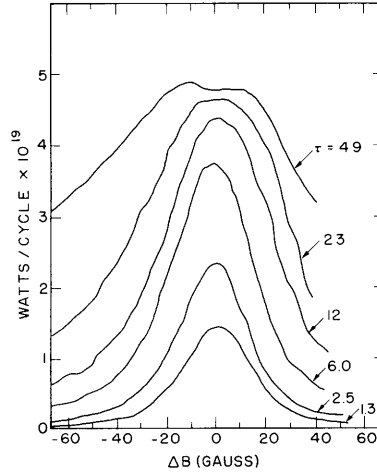


Fig. II-14. Effect of plasma opacity on line shape.

could be considerably greater than unity without violating the limitation mentioned above. The effect of increasing the optical depth αL is shown in Fig. II-14, where recorder traces of the emitted radiation are reproduced. The factor τ is the optical depth at the line center (that is, when $\omega_b = \omega$); it is adjusted by varying the electron density in the discharge that is being studied. Although τ changes by approximately a factor of 40, the height of the line only increases by approximately a factor of 3. At higher τ , we can detect the line asymmetry that characterizes the departure of the real part of the index of refraction from unity.

A convenient estimate of the optical depth can be made, in a dc discharge, as follows. At the line center, for a plasma column of arbitrary radial electron-density distribution placed axially along a waveguide, the radiated power is

$$p = kT\Delta f \frac{\iiint_{\text{plasma}} \alpha(x, y) E^2 e^{-\alpha z} dx dy dz}{\iint_{\text{waveguide}} E^2 dx dy}$$

where E is the electric field in the waveguide, which is assumed not to be greatly perturbed by the plasma (5). At resonance, for a wave traveling along the magnetic field directed along the waveguide axis,

$$\alpha(x, y) = \frac{n(x, y) e^2}{m\epsilon_0 c \left(1 - (\lambda/\lambda_c)^2\right)^{1/2}} \left\langle \frac{1}{v_c} \right\rangle$$

in which the brackets denote averaging over the electron velocity distribution function.

Furthermore, in the positive column of a dc discharge, the ratio of tube current I to electric field \mathcal{E} is

$$\frac{I}{\mathcal{E}} = \frac{e}{m} \left\langle \frac{1}{v_c} \right\rangle \int n(x, y) dx dy$$

We thus find, approximately, that

$$P = kT\Delta f(1 - e^{-\bar{a}L}) W[n(x, y)] \quad (4)$$

where

$$\bar{a} = \frac{1}{\epsilon_0 c} \frac{I}{A \mathcal{E}} \left(1 - (\lambda/\lambda_c)^2 \right)^{-1/2}$$

and

$$W[n(x, y)] = \frac{A \iint n(x, y) E^2 dx dy}{\iint n(x, y) dx dy \iint E^2 dx dy}$$

The cross-section area of the discharge is A , and we have approximated

$$\int e^{-a(x, y)z} dz \approx \frac{1 - e^{-\bar{a}L}}{\bar{a}}$$

as being independent of x and y . When $\bar{a}L \ll 1$, the result, with no such approximation, is

$$P = \frac{kT\Delta f}{\epsilon_0 c} \frac{I}{\mathcal{E}} \frac{2L}{\mathcal{A}} \frac{W[n(x, y)]}{\left(1 - (\lambda/\lambda_c)^2 \right)^{1/2}} \quad (5)$$

where \mathcal{A} is the waveguide cross-section area. Both Eqs. 4 and 5 are independent of $v_c(v)$.

The weighting factor $W[n(x, y)]$ is taken to be unity: For a 1-inch diameter discharge tube coaxial with a Type RG-48u waveguide ($3 \times 1 \frac{1}{2}$ inches), W equals 0.949 for a uniform density distribution, and 0.967 for a radial Bessel function distribution $J_0\left(2.405 \frac{r}{R}\right)$, where R is the radius of the tube. This is to be contrasted with the fact that the uniformly distributed distribution contains approximately twice as many electrons as the Bessel distribution, for the same central density at $r = 0$.

For a non-Maxwellian distribution, we replace kT in Eqs. 4 and 5 by $\left\langle \frac{mv_{\perp}^2}{3v_c} \right\rangle / \left\langle \frac{1}{v_c} \right\rangle$. For $v_c = \text{constant}$, the radiation is proportional to the average energy; otherwise it depends, but not too strongly, upon $v_c(v)$.

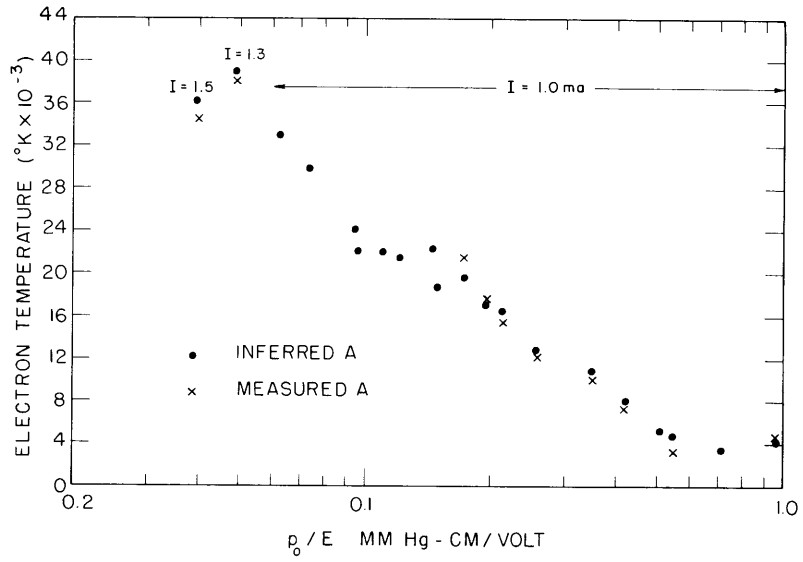


Fig. II-15. Measurements of electron temperature in low-current positive column.

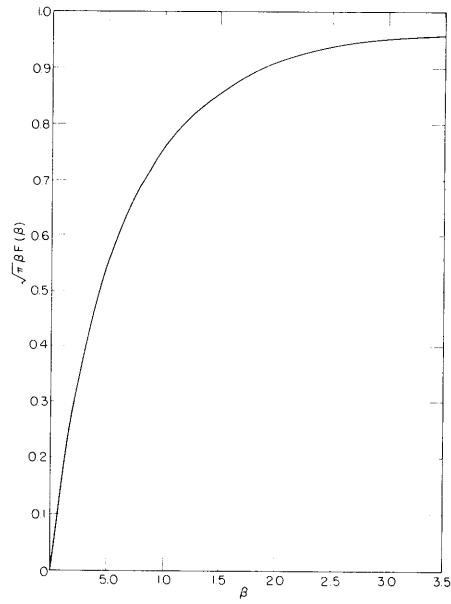


Fig. II-16. Correction to $\bar{\alpha}L$ when Doppler broadening is present.

Measurements of electron temperature made with the use of this method, in which the absorptivity A is inferred from the tube current and voltage, are shown in Fig. II-15. For comparison, results that depend upon a direct measurement of A are also shown (5).

When Doppler broadening is present, in addition to collision broadening, we see, from Eq. 3, that

$$a = \frac{\omega}{c} \frac{\omega_p^2}{\omega^2} \beta \frac{c}{v_T} \frac{1}{\sqrt{\pi}} \int_{-\infty}^{\infty} \frac{e^{-y^2}}{y^2 + \beta^2} dy = \sqrt{\pi} \frac{\omega_p^2}{\omega_b v_T} F(\beta)$$

where

$$F(\beta) = e^{\beta^2} \left[1 - \frac{2}{\sqrt{\pi}} \int_0^{\beta} e^{-x^2} dx \right]$$

Thus, when the Doppler effect is included, $\bar{a}L$ is equal to $\bar{a}L$ for collision broadening only, multiplied by $\sqrt{\pi}\beta F(\beta)$. This factor is shown in Fig. II-16. For large β , the factor approaches unity, but for $\beta < 2$, the opacity at resonance is a strong function of β .

Referring, again, to Fig. II-13, in which the experimental results were obtained with $\bar{a}L$ not small compared with unity, we see that correction for the opacity effect is dependent upon advance knowledge of β . This was obtained by measuring the absorptivity A and deducing β_a from $\sqrt{\pi}\beta_a F(\beta_a) = A/(\bar{a}L)$. The values of β_a that were used in opacity corrections are shown in Fig. II-13, and comparison with the values of β which best fit the data can be made. The relatively poor comparison is attributed mainly to the fast variation of the curve in Fig. II-16. The temperature values indicated in Fig. II-13 are obtained from the best fit β 's. Opacity corrections were obtained by solving for $\bar{a}L$:

$$\frac{h}{h_o} = \frac{1 - e^{-\bar{a}L}}{1 - e^{-H}}$$

where h is the height of the recorder trace, h_o is its value at line center, and H is the opacity at line center, measured independently.

d. Measurements of Doppler Shift of Cyclotron Radiation

Since the electrons that emit the cyclotron radiation have a net drift velocity v_d in a dc discharge, the radiation is Doppler-shifted by a frequency interval $\Delta\omega = \omega_b (v_d/v_\phi)$, where v_ϕ is the phase velocity of the radiation. Since $v_d \ll v_\phi$, the shifts are small and direct detection is difficult. However, by simultaneously receiving the radiation that is emitted both in, and opposite to, the drift, and by subtracting the two signals,

(II. PLASMA DYNAMICS)

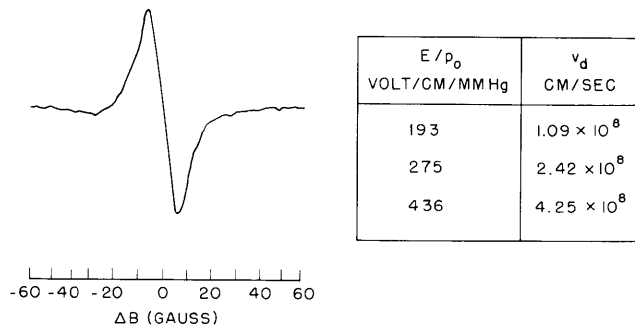


Fig. II-17. Doppler shift of cyclotron resonance radiation.

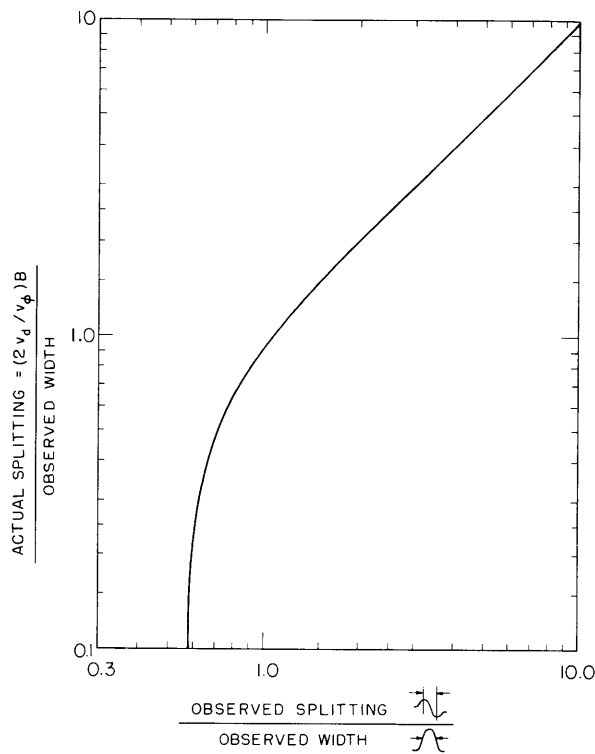


Fig. II-18. Electron drift velocity in terms of discriminator peak splitting and linewidth.

a discriminator pattern is produced, the spacing between the peaks of which, to first approximation, is $2\omega_b (v_a/v_\phi)$. Observations of such difference patterns were made, and a typical result is shown in Fig. II-17. Also shown are some values of v_d for electrons in helium, which were inferred from these Doppler-shift methods and the corresponding \mathcal{E}/p_0 .

The main disadvantage of this method arises when the Doppler shift is of the same

order as the linewidths. Subtracting one Lorentz line from another yields a resultant,

$$R = \frac{1}{(\Omega - \delta)^2 + \nu_c^2} - \frac{1}{(\Omega + \delta)^2 + \nu_c^2}$$

where $\Omega = \omega - \omega_b$, and $\delta = (v_d/v_\phi) \omega_b$. Differentiating R with respect to Ω to find the positions of the discriminator peaks Ω_2 , we find that

$$3 \frac{\left(\frac{\Omega_1}{2}\right)^2}{\delta^2} = \left(1 - \frac{\nu_c^2}{\delta^2}\right) + 2 \left[1 + \frac{\nu_c^2}{\delta^2} + \left(\frac{\nu_c^2}{\delta^2}\right)^2\right]^{1/2}$$

As $(\nu_c/\delta)^2 \rightarrow 0$, $\left(\frac{\Omega_1}{2}\right)^2 \rightarrow \delta^2$; but as $(\nu_c/\delta)^2 \rightarrow \infty$, $\left(\frac{\Omega_1}{2}\right)^2 \rightarrow \frac{1}{3} \nu_c^2$, independently of δ . This is shown in detail in Fig. II-18. Apparently, as δ/ν_c decreases, the peaks move together, at first, but stop at a value determined by ν_c , and then the relative heights decrease but do not come any closer together. Thus, for linewidths encountered in this particular experiment, Doppler shifts were not interpretable for $\left(\frac{v_d}{v_\phi}\right) \frac{\omega_b}{\nu_c} < 0.5$.

J. L. Hirshfield

References

1. J. L. Hirshfield, Microwave Radiation from Plasmas, Ph. D. Thesis, Department of Physics, M. I. T., 1960.
2. R. B. Dingle, Doreen Arndt, and S. K. Roy, Appl. Sci. Research, Sec. B, Vol. 6, p. 151, 1956.
3. A. G. Sitenko and K. N. Stepanov, Soviet Phys. -JETP 4, 512-520 (1957).
4. D. W. Posener, Australian J. Phys. 12, 184 (1959).
5. G. Bekefi, J. L. Hirshfield, and S. C. Brown, Phys. Rev. 116, 1051-1056 (1959).

5. HARMONICS OF CYCLOTRON RADIATION RESULTING FROM INHOMOGENEITY OF THE MAGNETIC FIELD

In the course of devising an experimental program to measure the synchrotron radiation from plasma electrons at moderate energies, low densities, and small ν_c/ω_b , estimates were made of the ratio of power radiated in the second harmonic to that radiated in the fundamental harmonic resulting from field inhomogeneity, in order to insure that this effect would not predominate over the synchrotron radiation.

With reference to Fig. II-19, the magnetic field is assumed to be in the z-direction, and is a function of y only. An electron is moving in the x, y plane. The equations of motion of the electron are

(II. PLASMA DYNAMICS)

$$m\ddot{x} = -e\dot{y}B \quad (1a)$$

$$m\dot{y} = e\dot{x}B \quad (1b)$$

where e is positive.

Integrating Eq. 1a once, and inserting the result in Eq. 1b, we obtain

$$\ddot{y} = -(e/m)^2 B \left[\int_{y_0}^y B(\zeta) d\zeta - (m/e)v_0 \right] \equiv -f(y) \quad (2)$$

Now

$$\ddot{y} = \frac{1}{2} \frac{d\dot{y}^2}{dy} \quad (3)$$

Inserting Eq. 3 in Eq. 2, integrating with respect to y , taking square roots, and integrating again with respect to t , we obtain

$$\int_{y_0}^y \frac{d\xi}{\left(-2 \int_{\xi_0}^{\xi} f(\eta) d\eta\right)^{1/2}} = t - t_0 \quad (4)$$

where the symbols η , ζ , and ξ are dummy variables of integration for y .

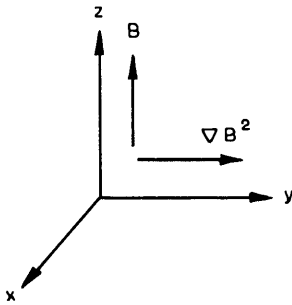


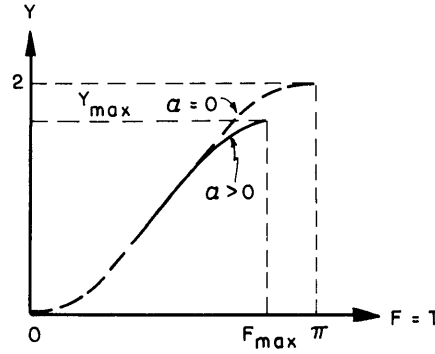
Fig. II-19. Orientation of the field and of the field gradient.

If we assume a linear variation of the magnetic field with y (which is a good approximation when the variation of the field is small over a Larmor orbit), that is,

$$B = B_0 + by \quad (5)$$

and that the initial conditions at $t = 0$ are: $x = 0$, $\dot{x} = v_0 = r_{bo}\omega_{bo}$, $y = 0$, $\dot{y} = 0$, then we obtain

$$f(y) = \omega_{bo}^2 \left\{ \left(1 - \frac{v_0}{\omega_{bo}} \frac{b}{B_0}\right) y + \frac{3}{2} \frac{b}{B_0} y^2 + \left(\frac{b}{B_0}\right)^2 \frac{y^3}{2} - \frac{v_0}{\omega_{bo}} \right\} \quad (6)$$

Fig. II-20. Illustration of $Y = G(a, T)$.

If we insert Eq. 6 in Eq. 4 and set $b = 0$, we obtain the equation of simple harmonic motion, which is a check on the correctness of Eqs. 6 and 4. That is, if

$$f(y) \rightarrow \omega_{bo}^2 y - v_o \omega_{bo}$$

and if we let $\xi' \equiv \xi - r_{bo}$, $\chi' \equiv \xi'/r_{bo}$, then

$$\begin{aligned} t &= \int_{-r_b}^{y'} \frac{d\xi'}{v_o \left[1 - (\xi'/r_{bo})^2 \right]^{1/2}} = \frac{1}{\omega_{bo}} \int_{-1}^{\chi'} \frac{d\chi'}{(1-\chi'^2)^{1/2}} \\ &= \frac{1}{\omega_{bo}} \left[\sin^{-1} \chi + \frac{\pi}{2} \right] \end{aligned}$$

or

$$y = r_{bo} \left[\sin \left(\omega_{bo} t - \frac{\pi}{2} \right) + 1 \right] = r_{bo} (1 - \cos \omega_{bo} t)$$

We define a new parameter a . From Eq. 5, $\Delta B = b \Delta y$ or

$$\frac{\Delta B}{B_o} = \left(\frac{b}{B_o} r_{bo} \right) \frac{\Delta y}{r_{bo}} \equiv a \frac{\Delta y}{r_{bo}} \quad (7)$$

where a is the fractional change in B over a Larmor orbit.

Equation 4 becomes

$$\omega_{bo} t = \int_0^{y/r_{bo}} \frac{dg}{\left(2 \left[g - \frac{(1-a)}{2} g^2 - \frac{a}{2} g^3 - \frac{a^2}{8} g^4 \right] \right)^{1/2}} \quad (8)$$

which is valid for $g \leq g_{\max} < 2$, where g is a dimensionless dummy variable.

(II. PLASMA DYNAMICS)

Thus, we have an expression $T \equiv \omega_{bo} t = F(\alpha, Y)$, with $Y \equiv y/r_{bo}$, and therefore we can obtain a function

$$Y = G(\alpha, T) \tag{9}$$

The function $G(\alpha, T)$ is an even function that can be expressed by a Fourier cosine series

$$G(\alpha, T) = A_0 + \sum_{\ell=1}^{\infty} A_{\ell} \cos \frac{\pi \ell T}{F_{\max}} \tag{10}$$

The solution for the amplitude of the ℓ^{th} harmonic of the y motion is

$$A_{\ell} = \frac{2}{F_{\max}} \int_0^{F_{\max}} G(\alpha, T) \cos \frac{\pi \ell T}{F_{\max}} dT \tag{11}$$

Figure II-20 illustrates Eq. 9 with α as a parameter, and $2F_{\max}$ is the dimensionless period of the motion.

The ratio of the power radiated by the second harmonic to that radiated by the first in the x -direction is

$$R = 16 \left(\frac{A_2}{A_1} \right)^2 \tag{12}$$

The values of R were evaluated for several values of α with the use of a digital computer. The results of the computations are listed in Table II-1.

Table II-1. Dimensionless period, F_{\max} ; dimensionless y amplitude, Y_{\max} ; Fourier coefficients A_0 , A_1 , and A_2 ; and power ratio R as functions of α .

α	F_{\max}	Y_{\max}	$2A_0$	A_1	A_2	R
0.1	2.886	1.832	1.795	-0.912	.018	.0063
0.05	3.002	1.909	1.889	-0.953	.012	.0026
0.01	3.121	1.981	1.989	-0.994	.005	.0004

An expression for the electron trajectory has also been derived. If we combine Eqs. 2 and 1b to express \dot{x} as a function of y , that is,

$$\dot{x} = \frac{m}{eB} \ddot{y} = -\frac{m}{eB} f(y)$$

then we obtain

$$\begin{aligned}
x &= -\left(\frac{m}{e}\right) \int_0^y \frac{f(\eta)}{B(\eta)} \frac{1}{\eta} d\eta = -\left(\frac{m}{e}\right) \int_0^y \frac{f(\eta) d\eta}{B(\eta) \left(-2 \int_0^\eta f(\xi) d\xi\right)^{1/2}} \\
&= -\left(\frac{e}{m}\right) \int_0^y \frac{\left[\int_0^\eta B(\xi) d\xi - \left(\frac{m}{e}\right) v_0\right] d\eta}{\left(-2 \int_0^\eta f(\xi) d\xi\right)^{1/2}} \quad (13)
\end{aligned}$$

When $B = B_0 + by = B_0 \left(1 + a \frac{y}{r_{bo}}\right)$, Eq. 13 becomes

$$\left(\frac{x}{r_{bo}}\right) = \int_0^{y/r_{bo}} \frac{\left[1 - (g + ag^2/2)\right] dg}{\left(2 \left[g - (1-a)g^2/2 - ag^3/2 - a^2g^4/8\right]\right)^{1/2}} \quad (14)$$

for $g \leq g_{\max} < 2$.

When $a \rightarrow 0$ Eq. 14 reduces to

$$(x/r_{bo})^2 + (y/r_{bo})^2 - 2(y/r_{bo}) = 0$$

which is the equation of a circle with center at $x = 0$, $y = r_{bo}$.

J. D. Coccoli

6. THERMAL RADIATION FROM AN ANISOTROPIC MEDIUM

Studies have been made in an effort to generalize the work of Rylov (1) for radiation from an anisotropic half-space to an isotropic half-space.

Rylov considers a medium of permeabilities ϵ and μ filling the space $z < 0$. In this space, he considers \vec{E} and \vec{H} to be Fourier-analyzed and decomposed into the "radiation" field \vec{E}_0 , \vec{H}_0 and the "reflected" field \vec{E}_r , \vec{H}_r that satisfy the inhomogeneous and homogeneous Maxwell equations, respectively

$$\begin{aligned}
\text{curl } \vec{E}_0 &= -ik\mu H_0 & \text{curl } \vec{E}_r &= -ik\mu \vec{H}_r \\
\text{curl } \vec{H}_0 &= ik\epsilon \vec{E}_0 + \frac{4\pi}{c} \vec{j}' & \text{curl } \vec{H}_r &= ik\epsilon \vec{E}_r
\end{aligned} \quad (1)$$

He then expands the waves $E_0 + E_r$ inside, and the wave E outside the medium in plane waves, and matches boundary conditions at $z = 0$

(II. PLASMA DYNAMICS)

$$\left. \begin{aligned} \vec{N} \times (\vec{E}_o + \vec{E}_r) \\ \vec{N} \times (\vec{H}_o + \vec{H}_r) \end{aligned} \right|_{z=0} &= \left. \begin{aligned} \vec{N} \times \vec{E} \\ \vec{N} \times \vec{H} \end{aligned} \right|_{z=0} \quad \text{div } \vec{E}_r = \text{div } \vec{E} = 0 \quad (2)$$

where \vec{N} is the unit vector normal to the plane $z = 0$. These six equations are sufficient to solve for the six unknowns, \vec{E} , \vec{H} . (Hereafter script letters will be indicated by underlining.)

This method is not immediately applicable to the anisotropic case because \vec{E}_r will not be transverse; instead, the divergence condition will be replaced by $\text{div } \hat{\epsilon} \cdot \vec{E}_r = 0$. This greatly complicates the solution, and so a more general method has been tried.

Consider the Green's tensor \hat{T} that satisfies the relation

$$\text{curl curl } \hat{T} - k^2 \hat{\epsilon} \cdot \hat{T} = 4\pi I \delta(\vec{r} - \vec{r}_o) \quad (3)$$

Bunkin (2) has shown that, for an infinite medium, T_{jk} may be written

$$T_{jk} = D_{jk}^! I_o(\vec{r}, \vec{r}_o) \quad (4)$$

where $D_{jk}^!$ is the adjoint of the differential matrix operator

$$D_{jk}^! = \frac{\partial^2}{\partial x_j \partial x_k} - \nabla^2 \delta_{jk} - k^2 \epsilon_{jk} \quad (5a)$$

and

$$I_o(\vec{r}, \vec{r}_o) = \frac{1}{(2\pi)^3} \int_{\infty} e^{ip_o(\vec{r} - \vec{r}_o)} \frac{d^3 p}{\Delta(\vec{p})} \quad (5b)$$

where $\Delta(\vec{p}) = \det(p^2 \delta_{ik} - p_i p_k - k^2 \epsilon_{ik})$.

For a noninfinite medium, the theory of dyadic Green's functions may be generalized (3), so that in the present case \hat{T} need not be symmetric. Carrying through this procedure, we write the solution for \vec{E} inside the medium

$$\vec{E} = \frac{k}{ic} \int_{z < 0} \hat{T} \cdot \vec{j} dv' - \frac{1}{4} \pi \iint [\hat{T} \cdot \vec{n} \times \text{curl } \vec{E} - (\hat{T} \text{ curl}) \cdot \vec{n} \times \vec{E}]_{z_o=0} ds_o \quad (6)$$

The field \vec{E} outside satisfies a homogeneous equation, and $\text{div } \vec{E} = 0$. Similarly, we obtain

$$\vec{E} = \frac{1}{4\pi} \iint [\underline{T} \cdot \vec{n} \times \text{curl}_o \vec{E} - (\underline{T} \text{ curl}_o) \cdot \vec{n} \times \vec{E}]_{z_o=0} ds_o \quad (7)$$

where \underline{T} is Green's tensor for the region outside.

We now take advantage of the fact that \hat{T} and \underline{T} are functions of $(\vec{r} - \vec{r}_o)$, and take a two-dimensional Fourier transform of Eqs. 6 and 7, using the convolution

theorem. We denote

$$\underline{\underline{E}}(z) = \frac{1}{2\pi} \int \underline{\underline{E}} e^{i\vec{p}_0 \cdot \vec{r}} dx dy$$

Then

$$\begin{aligned} \underline{\underline{E}}(z) &= \frac{2\pi k}{ic} \int_{-\infty}^0 \underline{\underline{T}}(z-z_0) \cdot \underline{\underline{j}}(z_0) dv_0 \\ &\quad - \frac{1}{2} [\underline{\underline{T}}(z) \cdot \underline{\underline{n}} \times \text{curl } \underline{\underline{E}}(0) - (\underline{\underline{T}}(z) \text{ curl}) \cdot \underline{\underline{n}} \times \underline{\underline{E}}(0)] \end{aligned} \quad (8)$$

$$\underline{\underline{E}}(z) = \frac{1}{2} [\underline{\underline{T}}(z) \cdot \underline{\underline{n}} \times \text{curl } \underline{\underline{E}}(0) - \underline{\underline{T}}(z) \text{ curl} \cdot \underline{\underline{n}} \times \underline{\underline{E}}(0)]$$

or in terms of the wave vectors $\underline{\underline{p}}$ and $\underline{\underline{p}}$,

$$\begin{aligned} \underline{\underline{E}}(z) &= \underline{\underline{F}}(z) - \frac{i}{2} [\underline{\underline{T}} \cdot \underline{\underline{n}} \times \underline{\underline{p}} \times \underline{\underline{E}} - \underline{\underline{T}} \times \underline{\underline{p}} \cdot \underline{\underline{n}} \times \underline{\underline{E}}] \\ \underline{\underline{E}} &= \frac{i}{2} [\underline{\underline{T}} \cdot \underline{\underline{n}} \times \underline{\underline{p}} \times \underline{\underline{E}} - \underline{\underline{T}} \times \underline{\underline{p}} \cdot \underline{\underline{n}} \times \underline{\underline{E}}] \end{aligned}$$

where

$$\underline{\underline{F}}(z) = \frac{2\pi k}{ic} \int_{-\infty}^0 \underline{\underline{T}}(z-z_0) \cdot \underline{\underline{j}}(z_0) dz_0$$

Thus

$$\begin{aligned} \underline{\underline{E}}(z) &= \underline{\underline{F}}(z) - \underline{\underline{T}}(z) \cdot \underline{\underline{Q}}_1 \cdot \underline{\underline{E}}(0) \\ \underline{\underline{E}}(z) &= \underline{\underline{T}}(z) \cdot \underline{\underline{Q}}_2 \cdot \underline{\underline{E}}(0) \end{aligned} \quad (9)$$

where

$$\underline{\underline{Q}}_1 = \frac{i}{2} \begin{bmatrix} p_3 - \underline{p}_3 & 0 & p_1 \\ 0 & p_3 - \underline{p}_3 & p_2 \\ \underline{p}_1 & \underline{p}_2 & 0 \end{bmatrix}$$

$$\underline{\underline{Q}}_2 = \frac{i}{2} \begin{bmatrix} \underline{p}_3 - p_3 & 0 & \underline{p}_1 \\ 0 & \underline{p}_3 - p_3 & \underline{p}_2 \\ p_1 & p_2 & 0 \end{bmatrix}$$

which has the solution:

(II. PLASMA DYNAMICS)

$$\vec{\underline{E}}(z) = \vec{\underline{T}}(z) \cdot \hat{Q}_2 \cdot \left(\vec{\underline{I}} + \vec{\underline{T}}(0) \cdot \hat{Q}_1 \vec{\underline{T}}(0) \cdot \hat{Q}_2 \right)^{-1} \vec{\underline{F}}(0) \quad (10)$$

Formally, the problem is solved; an inverse transform of this will yield $\vec{\underline{E}}(\vec{r})$. In practice, the integral in Eq. 5b and the inverse transform above (Eq. 10) will present serious difficulties.

The evaluation of Eq. 5b, or its equivalent, cannot be avoided. It is closely connected with the evaluation of the dispersion relation for the medium. This is equivalent to determining $\Delta(\vec{p})$ in Eq. 5b and is used when following a method analogous to Rytov's.

The general philosophy behind this procedure and how it relates to thermal radiation can be stated as follows: When the process that has been described is completed, we obtain

$$\begin{aligned} \vec{\underline{E}}(\vec{r}) &= \hat{O} \cdot \vec{j}(\vec{r}') \\ \vec{\underline{H}}(\vec{r}) &= \hat{O}' \cdot \vec{j}(\vec{r}') \end{aligned}$$

where \hat{O} and \hat{O}' are integral operators, and \vec{j} is considered to arise from thermal causes. The Poynting vector, $\text{Re } \vec{\underline{E}} \times \vec{\underline{H}}$, will then depend on $\langle \vec{j}(\vec{r}') \vec{j}(\vec{r}'') \rangle$, where the brackets denote an ensemble average. This dyadic is, to a good approximation, proportional to the unit dyadic multiplied by $\delta(\vec{r}' - \vec{r}'')$. The constant of proportionality contains the temperature dependence of the radiation. It is derived by applying the Nyquist noise theorem (4) to the continuous coordinate of \vec{j} . A more detailed study of this correlation of currents would come from a consideration of the kinetic equations for the radiating system.

D. E. Baldwin

References

1. S. M. Rytov, Theory of Electric Fluctuations and Thermal Radiation, translated by H. Erkku, AFCRC-TR-59-152, Air Force Cambridge Research Center, Bedford, Massachusetts, July 1959.
2. F. V. Bunkin, Soviet Phys. -JETP 5, 277 (1957); 5, 665 (1957).
3. P. M. Morse and H. Feshbach, Methods of Theoretical Physics (McGraw-Hill Book Company, New York, 1953), see Chapter 13.
4. L. D. Landau and E. M. Lifshitz, Macroscopic Electrodynamics (Addison-Wesley Publishing Company, Inc., South Reading, Mass., 1960).

II-B. PLASMA ELECTRONICS*

Prof. L. D. Smullin
Prof. H. A. Haus
Prof. A. Bers
Prof. D. J. Rose
P. Chorney

L. J. Donadieu
T. H. Dupree
T. J. Fessenden
W. D. Getty

L. M. Lidsky
A. Peskoff
S. D. Rothleder
R. C. Wingerson
S. Yoshikawa

1. HOLLOW-CATHODE DISCHARGE

A new name has been adopted for the system presented in Quarterly Progress Reports No. 56 and No. 57 as the "Low-Pressure Gas Arc." The "Hollow-Cathode Discharge" has evolved from the vacuum carbon arc developed at Oak Ridge National Laboratory for D_2^+ dissociation in the DCX Thermonuclear Experiment. Because the hollow-cathode discharge produces a steady, dense, highly ionized plasma with relatively simple equipment, it appears to be a valuable tool for the study of plasmas, as well as being an interesting object of study in itself. The study of the hollow-cathode discharge was initiated, last summer, at Oak Ridge National Laboratory and subsequently, at the Research Laboratory of Electronics. Two of these devices, which are substantially alike, are now in operation: one under Rose, and the other under Smullin.

The work of the two groups overlaps considerably. Most of the effort has gone into learning how to make the discharge run stably and into determining its gross operating characteristics. Not all of the results that will be quoted in the successive sections of this report are consistent; but we feel that these discrepancies will be ironed out as our work progresses. In the future, however, the work of the two groups will diverge. The primary interest of the group under Smullin will be in the study of the dynamic behavior of plasmas (reactive medium, amplification, and so forth), while the group under Rose will be more interested in the physics of the hollow-cathode discharge itself and in its use as a plasma source.

D. J. Rose, L. D. Smullin

2. EXPERIMENTAL RESULTS OF THE STUDY OF THE HOLLOW-CATHODE DISCHARGE

Experimental studies of the hollow-cathode discharge (1) consisted of the measurement of some of its basic properties and the development of dependable long-lived cathodes. We found that a thin-walled tantalum seamless tube, approximately 2 inches long, with an outside diameter of 5/32 inch, operates as a cathode with argon gas. (Tantalum and tungsten tubes with 1/16 inch outside diameter have also been successfully used.) With these cathodes, the discharge current can be varied from 2 to 80 amp. The maximum current is limited by the anode cooling system in the present discharge

*This work was supported in part by National Science Foundation under Grant G-9330.

(II. PLASMA DYNAMICS)

apparatus. However, as the current increases, the cathode temperature gradually approaches the melting temperature of tantalum, which therefore limits the current. The discharge is extinguished when the current is insufficient to heat the cathode to the required temperature.

The greatest advantage of the tantalum cathode is its relatively long life. The large-diameter tubes will operate for approximately 8 hours, whereas a carbon cathode runs for less than 30 minutes. During operation the wall thickness of the tantalum tube gradually decreases, and small holes that are scattered uniformly along the tube appear. The cathode continues to operate – even with several dozen of these pinholes present – until it is weakened enough to break off.

The stability of the discharge current and voltage, its appearance to the eye, and its ease of starting are unaffected by the change of cathode material. The metal cathodes require a slightly lower gas input flow rate than the carbon cathodes, and therefore their operating pressure is lower. The minimum flow rate for sustaining a discharge is less than 1 cc-atm per minute, and this flow rate maintains a pressure of 4×10^{-4} mm Hg in the main chamber.

In the rest of this report, data on the discharge characteristics are presented, with brief comments on possible conclusions to be drawn from these data. Tantalum cathodes and argon gas were used in all of these experiments.

a. Current-Voltage Static Characteristics

Typical static characteristics of the discharge are presented in Figs. II-21 and II-22. In Fig. II-21, voltage is plotted as a function of current with flow rate as a parameter. In Fig. II-22, current and voltage are plotted against flow rate. The discharge exhibits, roughly, two modes of operation. One mode is characterized by a low operating voltage, a high flow rate, and the appearance of an intense blue column, approximately 0.25 inch in diameter. The second mode is characterized by a high operating voltage, a low flow rate, and the partial disappearance of the blue column. In this mode, the column becomes larger in diameter and its edges are hazy and undefined. Curves 1 and 3 of Fig. II-21 are examples of these two modes. The transition from one mode to the other is continuous.

The static characteristics have a negative slope in the low-current range for all flow rates measured and therefore admit the possibility of an instability. However, we believe that the observed stability of the discharge in this current range may be attributable to the dependence of cathode temperature on the current. This dependence results in a stable, constant-current dynamic behavior. To first order, these properties are independent of the magnitude of the magnetic field between 300 and 1000 gauss.

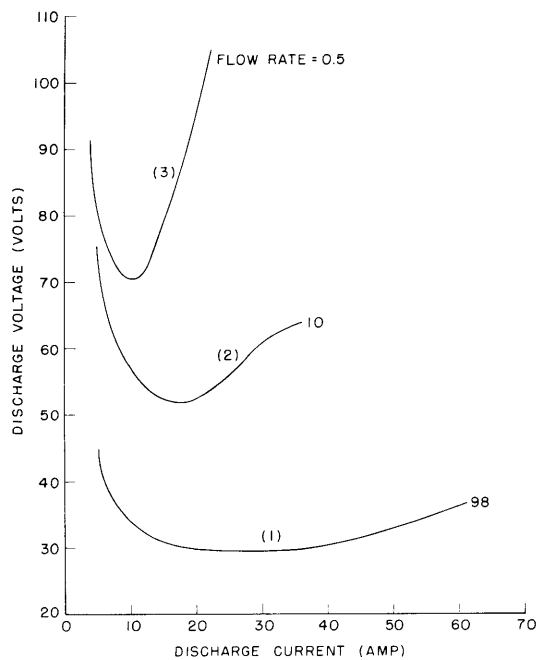


Fig. II-21. Voltage-current static characteristics. The parameter is the flow rate of argon in cc-atm/min.

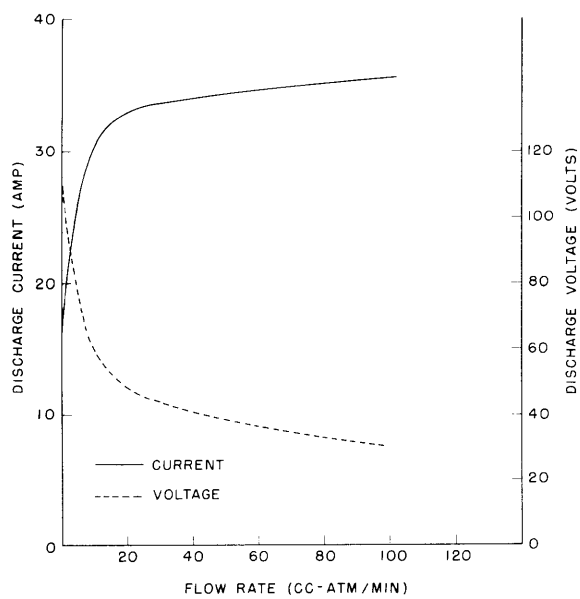


Fig. II-22. Discharge current and voltage dependence on flow rate.

(II. PLASMA DYNAMICS)

b. Anode Power Dissipation

The power dissipation in the anode was measured by calorimetric means for various values of current, magnetic field, and flow rate. The results shown in Table II-2 are divided into two groups according to the pressure in the discharge chamber, which is a known function of the flow rate. The voltage recorded as V_s is given by the difference between the total discharge voltage and the ratio of anode dissipated power to anode current. The voltage V_s is remarkably constant for each pressure group and is near the first ionization potential of argon (15.68 volts) in the high-pressure case and near the second ionization potential (27.76 volts) in the low-pressure case. This suggests that a cathode sheath voltage drop (V_s) approximately equal to the ionization potential of argon may exist, and that after leaving the cathode the electrons are accelerated toward the anode by the remaining voltage drop in an essentially collision-free stream. The electron density, calculated by assuming that all of the current is electron convection current in a beam of the same diameter as the cathode, is given in column 4 of Table II-2. The presence of an appreciable number of lower-energy electrons in the discharge would increase the value of the apparent density given in Table II-2.

Approximately 65 per cent of the total power input is dissipated in the anode. The percentage increases slightly in the low-pressure mode. Most of the remaining power is radiated by the hot cathode.

c. Radiofrequency Power Spectrum Measurements

Using radio receivers and a spectrum analyzer, we investigated the radiofrequency spectrum of the discharge in the 10-1000 mc frequency band. An attempt was made to eliminate stray effects caused by the coupling circuit between the discharge and the receiver antenna by constructing a coaxial transmission line. We used the cathode holder as the center conductor and the vacuum chamber casing as the outer conductor. The receiver input impedance was made equal to the characteristic impedance of this transmission line.

The results of these measurements indicate that the discharge generates noise power more or less uniformly over this frequency band. The measured noise is 20-30 db greater than the expected value of shot noise.

From conclusions based on the data in Table II-2, we assume that a large number of electrons is drifting through a stationary ion cloud with energies between 20 and 80 volts. Thus, the large observed noise levels may be due to interaction (amplification) between the electrons and ions.

Table II-2. Results of the measurement of anode power dissipation.

A. High-Pressure Mode. Pressure in discharge chamber = 1×10^{-3} mm Hg.

Discharge Voltage (volts)	Discharge Current (amp)	V_s (volts)	n (cm^{-3})
35	10	11	3×10^{12}
30.5	14.5	14	5×10^{12}
30	21	14	8×10^{12}
36	46.8	13	15×10^{12}
31	51.2	13	18×10^{12}
34.5	52.5	18	13×10^{12}

B. Low-Pressure Mode. Pressure in discharge chamber = 5×10^{-4} mm Hg.

Discharge Voltage (volts)	Discharge Current (amp)	V_s (volts)	n (cm^{-3})
90	14.7	32	3×10^{12}
93.5	18	34	4×10^{12}
109	18.5	33	2×10^{12}
120	20.7	35	3×10^{12}
88	22.8	31	5×10^{12}
93	23	33	3×10^{12}
98	23.4	34	3×10^{12}

(II. PLASMA DYNAMICS)

d. Reflection of Microwave Energy from the Discharge Column

A vacuum-tight circular waveguide, 2.5 inches in diameter, was inserted into the vacuum chamber through the front viewing port. The discharge column passed in and out of this waveguide through small holes. No difficulty was experienced in operating the discharge when the waveguide was not grounded. The object of the experiment was to determine whether or not the plasma would reflect or transmit microwave energy. The frequency range investigated was 7000-10,000 mc.

While the oscillator was mechanically swept through this band, the reflected power was obtained from a directional coupler and automatically recorded after detection. Runs were made with the discharge turned off and on. With the discharge turned off, the reflection occurs at the rear cover plate of the vacuum chamber, located 52 cm from the position of the discharge column and approximately the same distance from the directional coupler. With the discharge turned on, the plane of reflection moves to the vicinity of the discharge column. This indicates that the discharge column did reflect in this frequency band. The plasma frequency is apparently higher than 10,000 mc, which is in agreement with the electron densities given in Table II-2. More microwave experiments of this kind are being planned.

e. Injection of an Electron Beam into the Discharge

Figures II-23 and II-24 show the scheme used for injecting an electron beam into the discharge. In order to keep the discharge from destroying the gun, the gun is placed within the magnetic shield that also serves as the anode of the discharge. The strongly divergent magnetic field in the anode aperture causes the discharge to diverge rapidly. On the other hand, the high-energy (10 kv) electron beam has little difficulty in penetrating this magnetic barrier. In practice, with no bias on the gun, it may collect approximately 0.25 amp of a 10-20 amp discharge. If it is biased 50-150 volts negative with respect to the anode, the current to the gun can be made essentially zero.

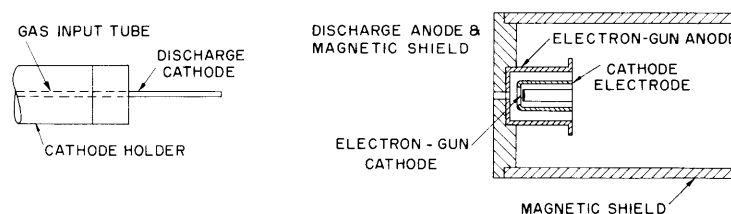


Fig. II-23. Schematic diagram of the discharge region of the hollow-cathode discharge showing the relative position of the discharge anode and the electron gun. (Channels for cooling water have been omitted.)

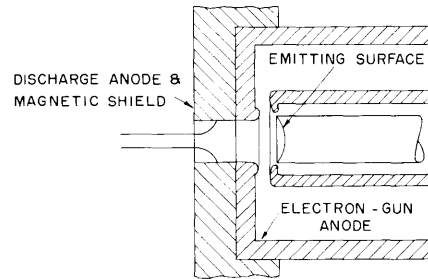


Fig. II-24. Enlarged view of the aperture in the hollow-cathode discharge anode where the electron beam is injected into the plasma. The rapid divergence of the magnetic-field lines effectively shields the electron-gun cathode from the discharge.

The gun that is used has a perveance of approximately 1.5×10^{-6} and has an impregnated cathode (2). After several hours of operation with the discharge on, the first gun is still usable.

The gun is driven at 10-15 kv by a 1- μ sec, 500-cps pulser. We plan to observe the effect of the beam on the rf noise in the discharge and on the visible spectrum.

W. D. Getty, L. D. Smullin

References

1. W. D. Getty, A low-pressure gas-arc device, Quarterly Progress Report No. 57, Research Laboratory of Electronics, M. I. T., April 15, 1960, pp. 27-29.
2. Several of these guns were kindly supplied to us by Dr. G. R. Brewer, of Hughes Aircraft Corporation, Culver City, California.

3. EXPERIMENTAL RESULTS ON THE HOLLOW-CATHODE DISCHARGE

The apparatus now in use is similar to that described by W. D. Getty in Quarterly Progress Report No. 57 (pages 27-29). A representative cathode is a 1/8 inch (inside diameter) thin-wall (0.005 inch-0.020 inch) tantalum tube approximately 2 inches in length. The anode, which plays a completely passive role, is usually a water-cooled copper disk, 1.25 inches in diameter. The axial magnetic field is maintained in the range of 300-850 gauss. The ambient pressure in the vacuum system is approximately $4-8 \times 10^{-4}$ mm, given by an input of approximately 0.5 cc-atm/sec of argon through the cathode tube. A discharge current of 40 amp was used for spectrographic investigations, and cathodes were run at this current from 3 to 4 hours with no visible sign of wear.

a. Qualitative Observations

(i) The hollow-cathode discharge will operate in the absence of magnetic field, once operation in the proper mode has begun. Of course, the external discharge spreads

(II. PLASMA DYNAMICS)

throughout the available volume.

(ii) The hollow-cathode discharge operates at currents as low as 10 amp and as high as 120 amp. This upper limit, which gives a current density of 1500 amp/cm^2 at the cathode orifice, was set by the external power supply and is no indication of the actual maximum current.

(iii) The hollow-cathode discharge will operate with a pure helium input. This is of interest for possible future application as an ion source because it suggests the possibility of generation of a hydrogenic plasma. Our present use of tantalum cathodes precludes the use of hydrogen.

(iv) In operation with a ring anode at currents of 20-80 amp, the visible beam extends for a distance of approximately 18 inches past the discharge region, breaking up only in the region of spreading magnetic field. Thus it is possible to generate a plasma in a field-free region.

b. Quantitative Measurements

The experiments performed in the brief period of operation may, albeit somewhat artificially, be split into two groups: investigation of the cathode mechanism and study of the plasma itself.

(i) Cathode Mechanism. A series of static volt-ampere characteristic curves were measured for various cathode configurations. A representative series of curves for argon input is presented in Fig. II-25. The two upper curves are obtained from cathodes of different wall thickness and thus from cathodes with differing internal

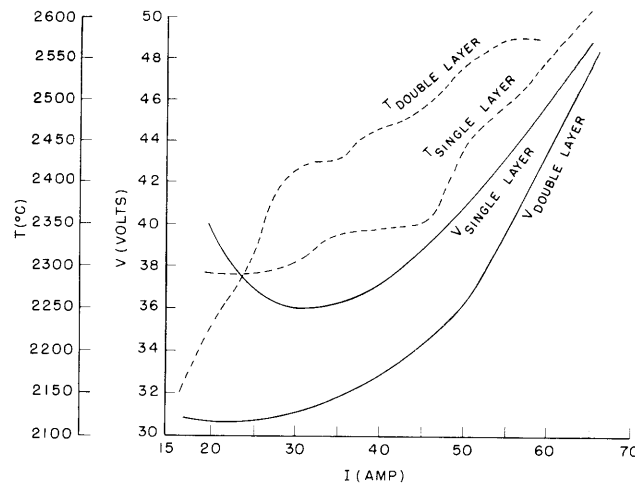


Fig. II-25. Static voltage and temperature versus current curves for argon feed rate of 0.5 cc-atm/sec. Cathode wall thickness, 0.010 inch. Double layer refers to two concentrically rolled 10-mil sheets giving a total wall thickness of 0.020 inch.

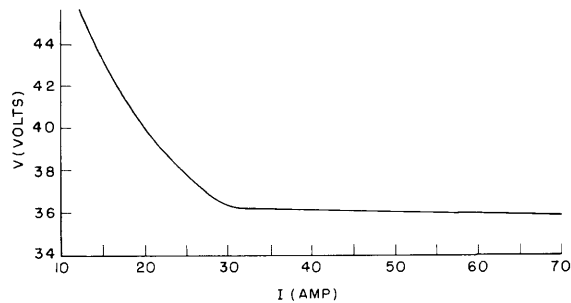


Fig. II-26. Static voltage and temperature versus current curves for helium feed rate of 0.5 cc-atm/sec. Cathode wall thickness, 0.010 inch.

temperature versus power characteristics. The temperature of the cathode orifice, as measured by an optical pyrometer, is plotted on the same graph. The different slopes for high and low current seem to indicate that at least two different mechanisms are operative.

A volt-ampere curve for pure helium input is presented in Fig. II-26. It is interesting to note that in the operation of the helium discharge an instability corresponding to a higher voltage mode of operation was found.

The gas pressure at the base of the cathode was measured at various gas-flow rates and was found to be several centimeters of mercury, giving particle densities inside the cathode of more than $10^{16}/\text{cm}^3$.

(ii) Plasma Properties. Since the chamber pressure was approximately $1/2 \mu$, and the pressure drop of a tube of the size of the cathode is small, it appears that the discharge within the cathode blocks the flow of neutral gas. The preliminary results of a set of pulsed probe measurements indicate that the charged-particle density in the main body of the plasma is in the range $2.6 \times 10^{13}/\text{cm}^3$ and is approximately 3×10^{11} at radial distances of 1 inch from the magnetically confined plasma column. The electrons in this external region appear to have an energy of approximately 2 ev. Measurements of electron energy in the main beam are masked by the large fraction of high-energy (30 ev) electrons streaming to the anode.

Several spectroscopic traces of the discharge were obtained by B. Bronfin for both helium and argon input. The spectrum for argon consists almost entirely of AII and AIII with less than $1:10^3$ of any impurity, including ionized cathode material. The helium spectrum, for which the transition probabilities are known, was utilized for temperature measurement. Most of the results substantiated the guess that the plasma is by no means in equilibrium. However, comparison of the intensities of the 3889 A, 4026 A, and 4713 A He I lines indicates a temperature of approximately 2.2 ev. Agreement with the energy found by probe measurement is probably fortuitous. However, these observations, combined with observations of lines requiring 51 ev for their production, indicate

(II. PLASMA DYNAMICS)

a low-energy (approximately 2 ev) body for the electron distribution plus a high-energy non-Maxwellian tail.

Doppler-shift measurements along the long axis of the beam have produced only the result that He^+ ions have an axial drift energy less than 2.5 ev.

c. Work in Progress

Experiments planned for the immediate future include an investigation of the emission mechanism with the use of finned and reflected cathodes and of a more accurate set of pulsed probe measurements. The possibility of obtaining a very high density plasma, suggested by the high particle density in the cathode, is being actively investigated. Another apparatus is now under construction.

D. J. Rose, L. M. Lidsky, S. D. Rothleder, S. Yoshikawa

4. STUDIES OF A HIGH-POWER PULSED MICROWAVE GAS DISCHARGE

A system was assembled for studying the properties of a gas discharge excited by high-level microwave power. Figure II-27 is a block diagram of the apparatus. A QK327 magnetron is used to generate a 10- μ -sec pulse of 1 Mw at a repetition rate of 60 pulses per second. The magnetron is tunable from 2696 mc to 2816 mc. A phase-shift type of power divider is used as the primary power control. The power divider is followed by a ferrite isolator, a directional coupler, a slotted section, and the resonant cavity within which the discharge takes place. The whole system can be pressurized with air or with sulfur hexafluoride to prevent breakdown.

Figure II-28 is a drawing of the resonant cavity showing the quartz tube that contains the discharge, and illustrates the method of coupling the cavity to the microwave system. The quartz tube is connected to a vacuum system that can be isolated from the pump and filled with hydrogen or helium. There is a small window in the cavity wall through which the light generated by the discharge can be observed. The total light or individual spectral lines can be observed as functions of time with the aid of a photomultiplier tube, a monochromator, and an oscilloscope. A small coupling loop is placed in the cavity to sample the microwave field inside the cavity.

A C-band probing system is coupled to the cavity to measure the perturbing effects of the discharge on the TE_{011} cavity mode. The C-band system contains a slotted section, the cavity wave meter, a directional coupler, a ferrite isolator, and a klystron oscillator.

With no discharge, the TE_{111} resonance of the cavity occurs at 2753 mc. At high-power levels, the discharge appears to act as a conductor, and the cavity has a higher-order coaxial mode (TE_{111}) resonance near 2730 mc (which would be the coaxial resonant frequency if the discharge were perfectly conducting). These two frequencies are close

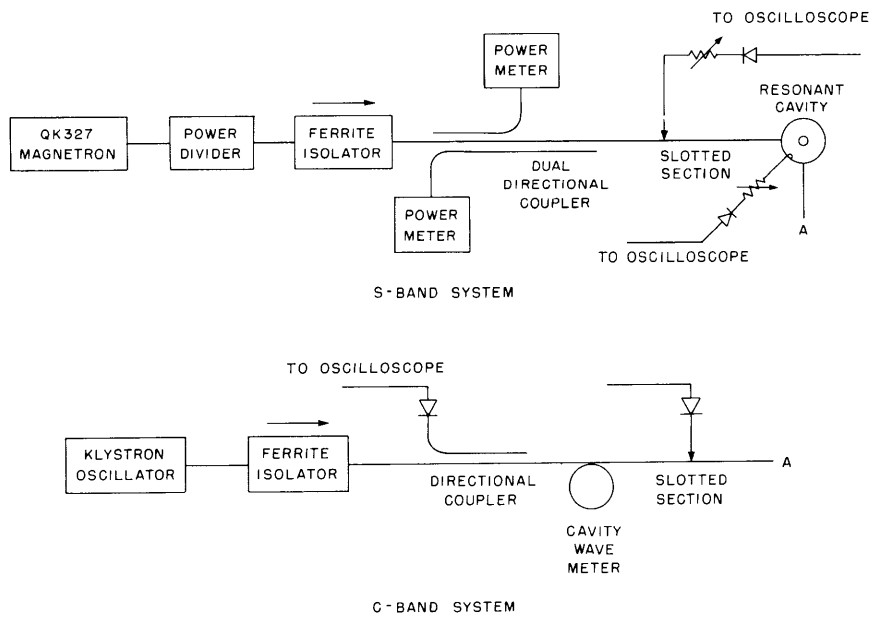


Fig. II-27. The microwave system.

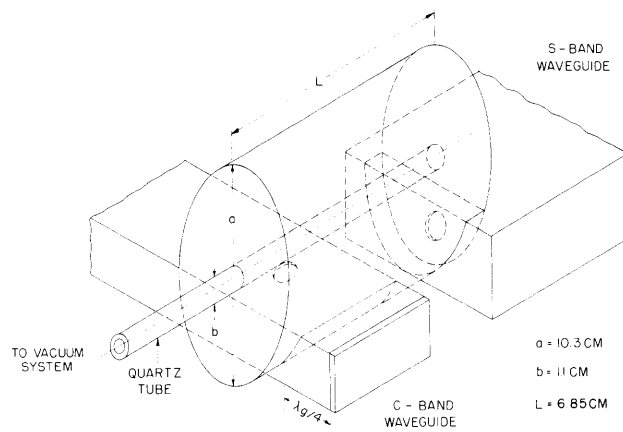


Fig. II-28. The resonant cavity.

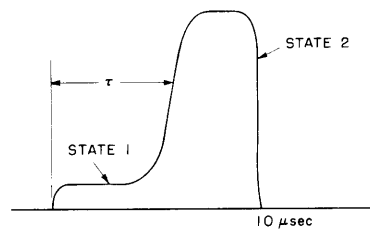


Fig. II-29. Sketch of the wave shape of the microwave field intensity inside the cavity versus time, showing a transition from state 1 to state 2 occurring at τ seconds.

(II. PLASMA DYNAMICS)

enough so that, with the magnetron tuned near 2730 mc, the discharge will start in the TE_{111} cavity mode and then shift to the coaxial mode.

Helium and hydrogen discharges at pressures of approximately 1 mm Hg have been studied at frequencies near the TE_{111} coaxial resonant frequency. For both gases, with the magnetron operating at frequencies slightly below 2730 mc, the discharge will operate in two stable states (see Fig. II-29). For relatively low values of incident power, the discharge operates in state 1 with almost all of the incident energy being reflected. As the incident power is increased, the absorbed power and field inside the cavity will jump suddenly to values several times larger than the values in state 1. The transition is first observed at the end of the 10- μ sec pulse, and, as the incident power is increased, the transition shifts smoothly toward the beginning of the pulse. In state 2, at constant frequency, the magnitude of the field in the cavity and the power absorbed by the discharge increase only slightly with incident power. Measurements of the frequency shift of the TE_{011} resonance indicate that the electron density is greater in state 2 than in state 1. (Electron densities are not reported because the existing theory (1) for determining electron density from the resonant frequency shift of this mode fails for the large shifts observed.)

The amount of incident power that is necessary for initiating a transition, and the resulting field inside the cavity, are dependent on the frequency of the incident energy. Figure II-30 is a plot of the relative fields of both states inside the cavity versus frequency of the incident power, for a constant time of transition ($\tau=6 \mu$ sec). The gas used was helium at a pressure of 0.92 mm Hg. It was impossible to obtain points nearer the critical frequency (2730 mc) because the microwave field of state 2 becomes large enough to break down the sulfur hexafluoride inside the cavity.

Figure II-31a, b, c, and d shows oscillograms of the field inside the cavity, the total light generated by the discharge, the 4471 helium line, and the 5056 silicon line. These oscillograms were taken of a helium discharge at a pressure of 1.9 mm Hg. The discharge was excited with 170 kw of peak incident power at a frequency of 2728 mc. The frequency response of the photo tube circuit used for obtaining oscillograms, Fig. II-31c and d, was insufficient to obtain accurate plots of light versus time. Stray pickup in the photo tube circuit accounts for the initial deflection of the oscilloscope trace shown in Fig. II-31d.

The shapes of other helium and silicon lines observed are similar to the oscillograms of Fig. II-31c and d. These oscillograms show that silicon is being strongly excited and that the helium lines are being quenched when the discharge is operating in state 2. This indicates that silicon may be absorbing a significant portion of the microwave energy and changing the characteristics of the discharge.

These phenomena will continue to be investigated. Electron-density and temperature measurements are planned. Microwave techniques will be used, and measurements will

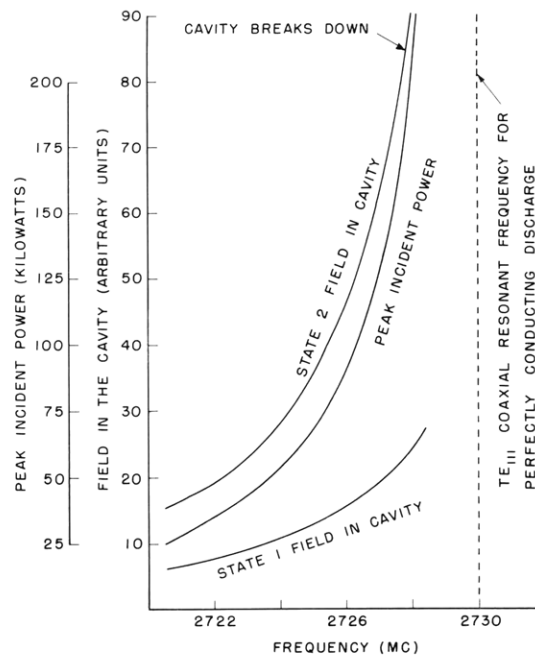


Fig. II-30. Plots of the magnitudes of the field in the cavity and the peak incident power versus frequency, showing values of the field with the discharge operating in state 1 and state 2. The time at which the transition occurred was held at 6 μ sec. The gas used was helium at a pressure of 0.92 mm Hg.

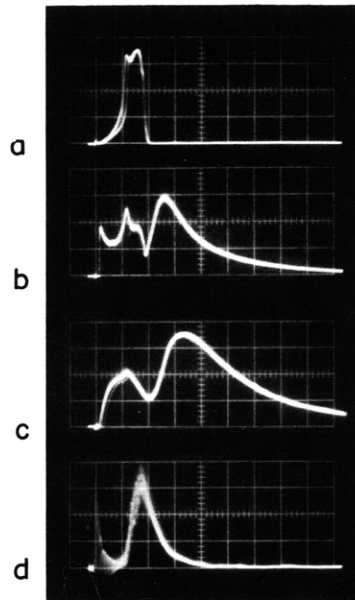


Fig. II-31. Oscillograms of a helium discharge in a resonant cavity showing wave shapes of: (a) the microwave field intensity inside the cavity; (b) the total light generated; (c) the 4471 helium line; and (d) the 5056 silicon line. A transition from state 1 to state 2 occurs at $\tau = 6 \mu$ sec. The time scale is 5 μ sec per large division.

(II. PLASMA DYNAMICS)

be compared with the energy absorbed by the discharge. From these measurements we shall attempt to determine the properties of dense plasmas produced by high-power microwave energy.

T. J. Fessenden

References

1. S. J. Buchsbaum and S. C. Brown, Microwave measurements of high electron densities, Phys. Rev. 106, 196-199 (1957).

5. THE EFFECT OF COLLISIONS ON PLASMA WAVEGUIDE PROPAGATION

The problem of propagation of small-signal oscillations in plasma waveguides has been solved by various authors under the assumption that there are no collisions. A perturbation method of evaluating the effect of very small collision frequency between electrons and neutral particles has been discussed (1, 2). In this report, we present a study, in more detail, of the effect of collisions on the propagation characteristics of a plasma waveguide. Collisions of electrons and neutrals, as well as of ions and neutrals, will be considered. In the basic formulation, no limitations are imposed on the magnitudes of the various collision frequencies; but we assume that collision frequencies are constant with particle velocity. We continue to use the usual assumption that there is no average drift velocity. We assume that the various charged particles experience only "collective" electrical forces and damping forces arising from collisions with neutrals. We consider a plasma composed of several species of particles. The total ac current caused by the motion of these various species is given by

$$\bar{\mathbf{J}} = \sum_n \bar{\mathbf{J}}_n = \sum_n \rho_{on} \bar{\mathbf{v}}_n \quad (1)$$

where $\bar{\mathbf{J}}_n = \rho_{on} \bar{\mathbf{v}}_n$ is the current of the n^{th} species, and $\bar{\mathbf{v}}_n$ is the small-signal ac velocity of that species.

When collisions with neutrals are taken into account, the small-signal force equation becomes

$$(j\omega + \nu_n) \bar{\mathbf{v}}_n = \eta_n \bar{\mathbf{E}} + \omega_{cn} \bar{\mathbf{v}}_n \times \bar{\mathbf{i}}_z \quad (2)$$

where ν_n is the collision frequency of the n^{th} species with neutrals; $\eta_n = q_n/m_n$, $\omega_{cn} = \eta_n B_0$; and $\bar{\mathbf{i}}_z$ is a unit vector in the direction of the axial dc magnetic field, B_0 . We need consider only the force equation to include the effect of collisions because the collision term does not appear in any of the other basic equations. When we multiply Eq. 2 by ρ_{on} , and recognize that $\bar{\mathbf{J}}_n = \rho_{on} \bar{\mathbf{v}}_n$, we obtain, after some manipulation,

$$j\omega\bar{\mathbf{J}}_n = \Omega_{pn}^2 \epsilon_0 \bar{\mathbf{E}} + \Omega_{cn} \bar{\mathbf{J}}_n \times \bar{\mathbf{i}}_z \quad (3)$$

where

$$\Omega_{pn}^2 = \frac{\omega_{pn}^2}{1 - j(\nu_n/\omega)} \quad (4)$$

$$\Omega_{cn} = \frac{\omega_{cn}}{1 - j(\nu_n/\omega)} \quad (5)$$

and

$$\omega_{pn}^2 = \frac{\eta_n \rho_0}{\epsilon_0} \quad (6)$$

Hence, we see that to include the effect of collisions, we simply substitute in the collisionless formulation of propagation in plasma waveguides, Ω_{pn}^2 for ω_{pn}^2 , and Ω_{cn} for ω_{cn} .

As an illustration of how collisions are included, we consider the quasi-static dispersion equation in a waveguide that is completely filled with a plasma composed of electrons, ions of one species, and neutrals. The collision frequency of electrons with neutrals is denoted ν_e , and ions with neutrals, ν_i . When collisions are ignored, we have the usual determinantal equation (3)

$$\beta_z^2 \left[\frac{\omega_{pi}^2}{\omega^2} + \frac{\omega_{pe}^2}{\omega^2} - 1 \right] = \beta_r^2 \left[1 + \frac{\omega_{pi}^2}{\omega_{ci}^2 - \omega^2} + \frac{\omega_{pe}^2}{\omega_{ce}^2 - \omega^2} \right] \quad (7)$$

When we include the effect of collisions, the determinantal equation becomes

$$\beta_z^2 \left[\frac{\Omega_{pi}^2}{\omega^2} + \frac{\Omega_{pe}^2}{\omega^2} - 1 \right] = \beta_r^2 \left[1 + \frac{\Omega_{pi}^2}{\Omega_{ci}^2 - \omega^2} + \frac{\Omega_{pe}^2}{\Omega_{ce}^2 - \omega^2} \right] \quad (8)$$

where

$$\Omega_{pi}^2 = \frac{\omega_{pi}^2}{1 - j(\nu_i/\omega)}, \quad \Omega_{pe}^2 = \frac{\omega_{pe}^2}{1 - j(\nu_e/\omega)}, \quad \Omega_{ci} = \frac{\omega_{ci}}{1 - j(\nu_i/\omega)}, \quad \Omega_{ce} = \frac{\omega_{ce}}{1 - j(\nu_e/\omega)}$$

and β_r is a constant determined by the radius of the waveguide. From Eq. 7, which was derived under the assumption of a dissipationless model, β_z^2 has poles and zeros at real values of ω . On the other hand, because of the damped motion caused by collisions, the poles and zeros of β_z^2 , given by Eq. 8, are located at complex frequencies.

(II. PLASMA DYNAMICS)

From Eq. 8, we observe that β_z^2 has 7 poles and 7 zeros. The locations of some of these poles and zeros, even under the assumption of small collision frequencies, ν_e and ν_i are difficult to determine. In the collisionless model, we see from Eq. 7 that β_z^2 has only 6 poles and 6 zeros. Two new critical frequencies, which are difficult to interpret, appear when collisions are included.

Because it is simpler and can be studied in more detail, a more instructive illustrative example is the quasi-static solution of the plasma-filled waveguide, in which the motion of the ions is disregarded. The dispersion in this system is given by the familiar relation (2, 4)

$$\beta_z^2 = \frac{\omega^2(\omega_{pe}^2 + \omega_{ce}^2 - \omega^2)}{(\omega_{pe}^2 - \omega^2)(\omega_{ce}^2 - \omega^2)} \beta_r^2 \quad (9)$$

when collisions are ignored. When we include collisions, Eq. 9 becomes

$$\beta_z^2 = \frac{\omega^2(\Omega_{pe}^2 + \Omega_{ce}^2 - \omega^2)}{(\Omega_{pe}^2 - \omega^2)(\Omega_{ce}^2 - \omega^2)} \beta_r^2 \quad (10)$$

Equations 9 and 10 each exhibit 4 poles and 4 zeros for β_z^2 . Furthermore, the location of the poles and zeros is symmetric with respect to the imaginary ω -axis; this is demonstrated when we substitute $s = j\omega$ and show that β_z^2 is a quotient of two polynomials in s , the coefficients in the polynomials being pure real.

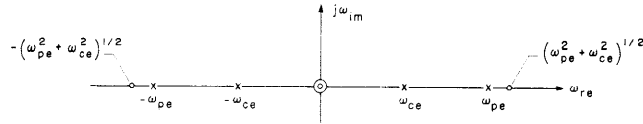


Fig. II-32. ω -plane plot of β_z^2 for electron plasma with no collisions.

Figure II-32 shows a typical ω -plane plot of the poles and zeros of β_z^2 for a collisionless system whose dispersion is governed by Eq. 9. Figure II-33 is a typical ω -plane of β_z^2 when collisions are considered, but with ν_e very much smaller than ω_{pe} . With the introduction of collisions, the poles and zeros of the collisionless model move off the real ω -axis into the complex plane. We must note that this plot is applicable only for ω very much greater than any of the ion quantities ω_{pi} , ω_{ci} , ν_i , since we have ignored the ion motion.

The approach used here to include collisions is more general than the perturbation approach (1,2), in that it can be applied when the motion of ions, as well as of electrons,

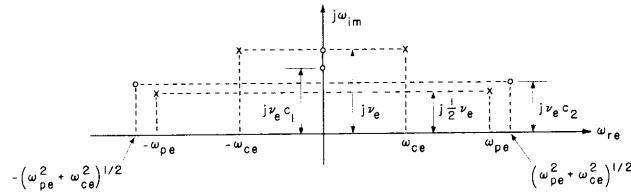


Fig. II-33. ω -plane plot of β^2 for electron plasma with small collisions: $\nu_c \ll \omega_{pe}$.

$$\text{The scale factor: } c_1 = \frac{\omega_{pe}^2}{\omega_{pe}^2 + \omega_{ce}^2}, \text{ and } c_2 = \frac{1}{2} \left(1 + \frac{\omega_{ce}^2}{\omega_{pe}^2 + \omega_{ce}^2} \right).$$

is considered. Furthermore, our approach, when applied to systems in which the ion motion is ignored, gives more reliable results than the perturbation approach because the basic assumptions of the perturbation approach are too restrictive. For instance, the perturbation approach predicts infinite attenuation when the collisionless β_z^2 is infinite, and it also stipulates that the propagating (real) part of β_z shall remain unperturbed because of small collisions. The present formulation shows that the attenuation constant, as well as the propagation constant, is finite for real frequencies in the vicinity of ω_{ce} and ω_{pe} .

P. Chorney

References

1. P. Chorney, Attenuation in ion-loaded waveguides, Quarterly Progress Report No. 53, Research Laboratory of Electronics, M. I. T., April 15, 1959, pp. 57-59.
2. A. W. Trivelpiece and R. W. Gould, Space-charge waves in cylindrical plasma columns, J. Appl. Phys. 30, 1784-1793 (1959).
3. P. Chorney, Propagation in plasma waveguides, Quarterly Progress Report No. 56, Research Laboratory of Electronics, M. I. T., Jan. 15, 1960, pp. 39-41.
4. P. Chorney, Electron-Stimulated Ion Oscillations, Technical Report 277, Research Laboratory of Electronics, M. I. T., May 26, 1958.

6. PHENOMENOLOGICAL LAW FOR SUPERCONDUCTIVITY, CHARACTERISTIC DEPTH, AND SUPERCURRENT

In connection with our program for producing a large superconducting solenoid, we have developed a phenomenological interpretation for the characteristic depth of the supercurrent.

Our approach is an extension of the Gorter-Casimir theory of thermodynamics, with the result (in mks units):

(II. PLASMA DYNAMICS)

$$B_c = \left(\frac{\gamma \mu_o}{2V_a} \right)^{1/2} T_c \left[1 - \left(\frac{T}{T_c} \right)^2 \right] \quad (1)$$

This is the parabolic law for the critical field B_c versus the temperature T , where γ is the electronic specific heat, V_a is the atomic volume, and T_c is the critical temperature.

The free energy of the reaction – normal state to superstate – is

$$G_N - G_S = \frac{V_a}{2\mu_o} \left(B_c^2 - B^2 \right) \quad (2)$$

Our main hypothesis identifies this free energy with the translational kinetic energy of the superconducting electrons, since free energy implies work done. Because the lattice atoms are much heavier than the electrons, the lattice contribution to free energy can be neglected. Hence

$$E_T = \frac{1}{2} m v_D^2 A N_c P_s \quad (3)$$

where v_D is the drift speed, A is Avogadro's number, N_c is the concentration of conduction electrons (density of the conduction band), and P_s is the probability that a conduction electron is in the superstate.

On the other hand, the current density j is related to the electron drift velocity by

$$j_s = e \frac{A N_c P_s}{V_a} v_D \quad (4)$$

Combining these equations, we obtain

$$j_s = \frac{1}{\left[\frac{V_a}{A N_c P_s} \frac{m}{e^2 \mu_o} \right]^{1/2}} \frac{\left(B_c^2 - B^2 \right)^{1/2}}{\mu_o} \quad (5)$$

The bracket in the denominator is a characteristic length

$$\lambda_s = \left[\frac{V_a}{A N_c P_s} \frac{m}{e^2 \mu_o} \right]^{1/2} \quad (6)$$

and the phenomenological law for the supercurrent is written

$$j_s = \frac{1}{\lambda_s \mu_o} \left(B_c^2 - B^2 \right)^{1/2} \quad (7)$$

Equation 7 should be used in place of Ohm's law for the solution of electrodynamic problems.

A vector meaning is attached to Eq. 7 because the $G_N - G_S$ term involves work; j_s and B are perpendicular to each other.

The phenomenological law will apply only in the range

$$0 < |B| < B_c \quad (8)$$

The right-hand inequality is obvious; the other condition arises because the direction of j cannot be defined if $B = 0$.

The probability P_s , as derived from the thermodynamics of the reaction, is

$$P_s = \frac{1}{1 + \exp\left[-\frac{1}{RT} \frac{V_a}{2\mu_0} (B_c^2 - B^2)\right]} \quad (9)$$

For $T \geq 0.1 T_c$ (which is true in practice) $P_s \approx 1/2$.

Equation 2 indicates that the effect of the magnetic field is to decrease the total energy, $(V_a/2\mu_0) B_c^2$, of the reaction by the amount $(V_a/2\mu_0) B^2$. We assume that this decrease corresponds to a conversion of energy into rotational energy of the superconducting electrons. Then we may write

$$\frac{V_a B^2}{2\mu_0} = \frac{AN_c P_s m v^2}{2} = \frac{AN_c P_s e^2 r_L^2 B^2}{2m} \quad (10)$$

where r_L is the Larmor radius. Equation 10 yields

$$r_L = \left[\frac{V_a}{AN_c P_s} \frac{m}{e^2 \mu_0} \right]^{1/2} = \lambda_s \quad (11)$$

which shows that the characteristic length of the phenomenological law (Eq. 7) is effectively the Larmor radius of superconducting electrons.

Penetration depth and current-sheet thickness are obtained straightforwardly as $d_c = (\pi/2) \lambda_s$. This approach leads naturally to a value of the characteristic length and provides a physical meaning for it, whereas the concept was introduced arbitrarily in London's theory of superconductivity. Also we find a bridge between thermodynamics and the electrostatics of superconductivity.

L. Donadieu

C. PLASMA MAGNETOHYDRODYNAMICS AND ENERGY CONVERSION*

Prof. O. K. Mawardi	G. W. Bukow	A. T. Lewis
Prof. H. H. Woodson	L. Y. Cooper	J. K. Oddson
Prof. J. A. Fay	R. S. Cooper	J. P. Penhune
Prof. W. D. Jackson	D. M. Dix	E. S. Pierson
Prof. D. C. Pridmore-Brown	D. A. East	J. W. Poduska
Dr. R. Gajewski†	W. H. Heiser	K-F. Voyerli
T. I. Sundström	G. B. Kliman	B. Zauderer

Work supported by the Aeronautical Accessories Laboratory, Wright Air Development Division, Wright-Patterson Air Force Base, Ohio, under Air Force Contract AF33(616)-3984, Project 8149, Task No. 61098 is now included in the activities of the Research Laboratory of Electronics. The report quoted below summarizes research conducted in the Electronic Systems Laboratory, M. I. T., under this contract, which has been in force since 1 February 1957, lists all publications to date, and deals in detail with the work undertaken during the period 1 February 1959 to 31 January 1960: "Summary Report: Study of Electrical Energy Conversion Systems for Future Aircraft," WADD Technical Report 60-148, 1 February 1960; H. H. Woodson and W. D. Jackson, Editors.

H. H. Woodson, W. D. Jackson

1. REFLECTION OF SHOCK BY A MAGNETIC FIELD

A theory has been developed for describing the experimental situation in which a strong gasdynamic shock wave is propagating into a region of magnetic field that is primarily perpendicular to the direction of motion of the shock. The magnetic Reynolds number (R_m) is presumed to be large. An idealized one-dimensional case is considered as the basis for the theory, and some qualitative remarks are made concerning the application of the theory to a case in which the magnetic field is generated by an electromagnet. A more lengthy treatment of a shock interaction with a magnetic field has been given by J. M. Burgers (1).

a. Experimental Model

We consider a one-dimensional magnetic field perpendicular to the x-axis so that $B = B_0$ for $x > 0$, and $B = 0$ for $x < 0$. The whole space contains a gas with a known initial state: density ρ_0 , pressure p_0 . This configuration requires a surface current of density B_0/μ_0 in the plane $x = 0$ to satisfy Maxwell's equations. Furthermore, we have to introduce formally a fictitious balancing pressure on the same plane to maintain equilibrium. As the strong shock wave propagates along the negative x-axis, it ionizes

* This work was supported by National Science Foundation under Grant G-9330; in part by Contract AF19(604)-4551 with Air Force Cambridge Research Center; and in part by WADD Contract AF33(616)-3984.

† Sloan Foreign Postdoctoral Fellow, from the Institute for Nuclear Research, Warsaw, Poland.

(II. PLASMA DYNAMICS)

the gas behind it. We consider the conductivity of the plasma behind the shock to be infinite. Upon striking the plane $x = 0$, the shock wave causes the current sheet to move in the positive x -direction. Consequently, the current density in the sheet is increased,

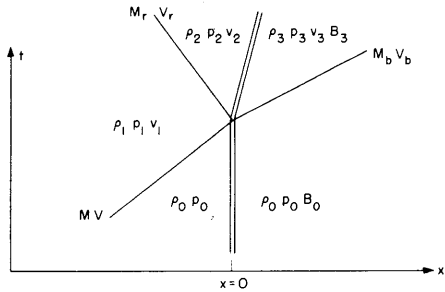


Fig. II-34. Time-distance diagram of shock interaction with magnetic field.

and a braking pressure is exerted on the plasma. During this interaction the current sheet remains a perfect contact discontinuity because of the infinite conductivity. This is a good approximation for $R_m > 1$.

The interaction between the plasma and the magnetic field gives rise to compression waves propagating both forward and backward from the interface. If the interaction is strong enough, these waves are superposed in both directions and shock waves are generated; the forward

traveling (refracted) shock is magnetohydrodynamic, the backward traveling (reflected) shock is gasdynamic. The increase of current density in the interface resulting from its motion is matched by an oppositely directed surface current in the magnetohydrodynamic shock front. This situation is illustrated in Fig. II-34, which shows a time-distance diagram. The notation that will be used hereafter is indicated in the figure.

b. Effect of Fringed Magnetic Field

The model for the one-dimensional case includes a current layer, and a balancing pressure that is artificially introduced in the contact discontinuity. Because the magnetic field generated by an electromagnet is irrotational it cannot be treated in a one-dimensional way. Nevertheless, this model is still applicable if the following conditions are fulfilled: (a) The perpendicular component of B is small for $x < 0$, and is equal to B_0 for $x > 0$. (b) The gradient of this component is large only within a small region close to the plane $x = 0$. (c) The shock propagates from infinity. (d) The electric conductivity is high enough to prevent the fringed magnetic field from penetrating the plasma. At the very moment when the shock front passes $x = 0$ the current sheet really exists, and the balancing pressure need not be invoked. The error introduced by applying the one-dimensional theory to a practical case can be reduced when the experimental conditions fulfill these requirements.

c. Governing Equations

If the energy of dissociation and ionization is only a small fraction of the internal energy in the heated plasma (which is true for a strong shock in hydrogen), the equations

for an ideal gas can be applied. Other governing equations are the relations for conservation of mass, momentum, and energy, and Walen's relation. The interaction is assumed to be so strong that all of the three transitions are shock transitions. The boundary conditions at the contact discontinuity are: $v_2 = v_3$, and $p_2 = p_3 + B_3^2/2\mu_0$.

In order to derive expressions for these quantities, we begin from the following transition relations for the incident (strong) shock, the reflected shock (2), and the refracted hydromagnetic shock (3).

Incident Shock:

$$\rho_1 = \rho_0 \frac{\gamma + 1}{\gamma - 1}$$

$$p_1 = p_0 \frac{2\gamma}{\gamma + 1} M^2$$

$$v_1 = \frac{2Mc}{\gamma + 1}$$

where $c = \left(\frac{\gamma p_0}{\rho_0}\right)^{1/2}$ is the velocity of sound, and γ is the ratio of specific heats.

Reflected Shock:

$$\rho_2 = \rho_1 \frac{1}{1 - \frac{2}{\gamma + 1} \left(1 - \frac{1}{M_r^2}\right)}$$

$$p_2 = p_1 \left\{ 1 + \frac{2\gamma}{\gamma + 1} (M_r^2 - 1) \right\}$$

$$v_2 = v_1 \left\{ 1 - \frac{M_r [2\gamma(\gamma + 1)]^{1/2}}{\gamma + 1} \left(1 - \frac{1}{M_r^2}\right) \right\}$$

Refracted Shock:

$$p_3 = p_0 \left\{ 1 + \frac{\gamma \left(\frac{\rho_3}{\rho_0} - 1\right) \left\{ 1 + \frac{\gamma - 1}{4S} \left(\frac{\rho_S}{\rho_0} - 1\right)^2 \right\}}{1 - \frac{\gamma - 1}{2} \left(\frac{\rho_3}{\rho_0} - 1\right)} \right\}$$

where $S = \frac{\gamma p_0 \mu_0}{B_0^2} \approx$ ratio of gasdynamic to magnetic energy density.

(II. PLASMA DYNAMICS)

$$v_3 = C_o \left(1 - \frac{1}{\rho_3/\rho_o}\right) \left[\frac{\rho_3}{\rho_o} \frac{1 + S + \frac{2 - \gamma}{2} \left(\frac{\rho_3}{\rho_o}\right) - 1}{(1+S) \left\{1 - \frac{\gamma - 1}{2} \left(\frac{\rho_3}{\rho_o}\right) - 1\right\}} \right]^{1/2}$$

where $C_o = \left(\frac{\gamma p_o}{\rho_o} + \frac{B_o^2}{\mu_o \rho_o}\right)^{1/2}$ is the characteristic velocity for region $x > 0$.

Velocity Condition:

$$\frac{2Mc}{\gamma + 1} \left\{ 1 - \frac{M_r [2\gamma(\gamma + 1)]^{1/2}}{\gamma + 1} \left(1 - \frac{1}{M_r^2}\right) \right\} = C_o \left(1 - \frac{1}{\rho_3/\rho_o}\right) \left[\frac{\rho_3}{\rho_o} \frac{1 + S + \frac{2 - \gamma}{2} \left(\frac{\rho_3}{\rho_o} - 1\right)}{(1+S) \left\{1 - \frac{\gamma - 1}{2} \left(\frac{\rho_3}{\rho_o} - 1\right)\right\}} \right]^{1/2}$$

Pressure Condition:

We observe that according to Walen's relation, this condition can be written:

$$\frac{p_2}{p_o} - \frac{\gamma}{2S} \left(\frac{\rho_3}{\rho_o}\right)^2 = \frac{p_3}{p_o}$$

or

$$\frac{2\gamma M^2}{\gamma + 1} \left\{ 1 + \frac{2\gamma}{\gamma + 1} (M_r^2 - 1) \right\} - \frac{\gamma}{2S} \left(\frac{\rho_3}{\rho_o}\right)^2 = 1 + \frac{\gamma \left(\frac{\rho_3}{\rho_o} - 1\right) \left\{ 1 + \frac{\gamma - 1}{4S} \left(\frac{\rho_3}{\rho_o} - 1\right)^2 \right\}}{1 - \frac{\gamma - 1}{2} \left(\frac{\rho_3}{\rho_o} - 1\right)}$$

A slightly modified form of these conditions lends itself better to numerical solutions:

$$M_r - \frac{1}{M_r} = \frac{\gamma + 1}{[2\gamma(\gamma + 1)]^{1/2}} - \frac{C_o(\gamma + 1)^2}{2Mc[2\gamma(\gamma + 1)]^{1/2}} \left(1 - \frac{1}{\rho_3/\rho_o}\right) \left[\frac{\rho_3}{\rho_o} \frac{1 + S + \frac{2 - \gamma}{2} \left(\frac{\rho_3}{\rho_o} - 1\right)}{(1+S) \left\{1 - \frac{\gamma - 1}{2} \left(\frac{\rho_3}{\rho_o} - 1\right)\right\}} \right]^{1/2}$$

$$M_r^2 = 1 - \frac{\gamma + 1}{2\gamma} + \frac{(\gamma - 1)^2}{4\gamma^2 M^2} + \frac{(\gamma - 1)^2}{8\gamma S M^2} \left(\frac{\rho_3}{\rho_o}\right)^2 + \frac{(\gamma + 1)^2}{4\gamma M^2} \cdot \frac{\left(\frac{\rho_3}{\rho_o} - 1\right) \left\{ 1 + \frac{\gamma - 1}{4S} \left(\frac{\rho_3}{\rho_o} - 1\right)^2 \right\}}{1 - \frac{\gamma - 1}{2} \left(\frac{\rho_3}{\rho_o} - 1\right)}$$

(II. PLASMA DYNAMICS)

As we expected, we found that the velocity of the transmitted shock is always greater than that of the initial shock. If $p_o \ll B_o^2/2\mu_o$ and $M \gg 1$, a common parameter of the two equations is B_o/M . The strength of the reflected shock is always very weak, but it increases slightly as B_o/M increases, and accordingly the strength of the transmitted shock decreases. However, it might be observed that although the Alfvén Mach number is decreased, the velocity of the transmitted shock is increased. For a constant strength of the incident shock an increase of the magnetic field therefore implies an increase of the velocity of both the reflected and the refracted shock. Table II-3 gives a few figures (mks units) that illustrate the situation for $p_o = 1$ mm Hg of hydrogen gas and initial shock Mach number 80 (shock velocity = 10^5 m/sec).

Table II-3.

B_o	B_o/M	M_r	M_b	V_b
0.3	3.75×10^{-3}	1.02	4.32	1.06×10^5
0.6	7.50×10^{-3}	1.06	2.38	1.17×10^5
1.2	15.0×10^{-3}	1.18	1.46	1.44×10^5
1.8	22.5×10^{-3}	1.33	1.17	1.73×10^5

The theory ceases to be applicable when the magnetic field becomes so strong that the characteristic velocity of the hydromagnetic medium is of the same magnitude as the initial shock velocity.

T. I. Sundström

References

1. J. M. Burgers, The Penetration of a Shock Wave into a Magnetic Field, Technical Note BN-102, University of Maryland, June 1957.
2. A. H. Shapiro, The Dynamics and Thermodynamics of Compressible Fluid Flow (Ronald Press Company, New York, 1953).
3. Z. J. J. Stekly, Magnetohydrodynamic Waves in a Transverse Magnetic Field, Sc. D. Thesis, Department of Mechanical Engineering, M. I. T., September 1959.

2. AN APPROXIMATE METHOD OF SOLUTION OF A TWO-DIMENSIONAL, LAMINAR MAGNETOHYDRODYNAMIC BOUNDARY LAYER WITH AN ARBITRARY PRESSURE GRADIENT

The Pohlhausen method (1) as applied to nonconducting fluids has been adapted to electrically conducting fluids. The boundary-layer momentum integral equation

(II. PLASMA DYNAMICS)

has the form

$$\frac{\tau_o}{\rho} = \frac{dU}{dx} \left[1 + \frac{\sigma B_{\perp}^2}{\rho \frac{dU}{dx}} \right] U \delta^* + \frac{d}{dx} [U^2 \theta] \quad (1)$$

where σ is the electric conductivity, and B_{\perp} is the component of the magnetic induction normal to the flow. The other variables have been defined by Schlichting (1). In addition to the usual boundary-layer approximations, the restrictions on this equation are that B_{\perp} and σ not vary over the boundary-layer thickness at any given x , and that the electric field not vary over distances comparable to the boundary-layer thickness. Suitable electric-current boundary conditions must be present to maintain the two-dimensional nature of the flow. Equation 1 also applies when there is a relative velocity between the magnetic field and the wall.

Following Pohlhausen, a polynomial of the fourth degree with arbitrary coefficients is now postulated for the boundary-layer velocity profile. If the force boundary condition at the wall is modified for the $\sigma(\underline{E} \times \underline{B})$ force, the results for $\frac{u}{U}$, $\frac{\delta^*}{\delta}$, and $\frac{\tau_o \delta}{\mu U}$ are the same as Pohlhausen's, provided that the Pohlhausen shape factor $\Lambda = \frac{\delta^2}{\nu} \frac{dU}{dx}$ is replaced by the generalized shape factor

$$\Lambda^* = \frac{\delta^2}{\nu} \frac{dU}{dx} \left[1 + \frac{\sigma B_{\perp}^2}{\rho \frac{dU}{dx}} \right]$$

If this profile is inserted in the momentum equation, the result is

$$\frac{d\theta}{dx} = \frac{1}{2} \frac{F(\Lambda^*)}{\frac{U\theta}{\nu}} + 2 \frac{\sigma B_{\perp}^2 \theta}{\rho U}$$

The function

$$F(\Lambda^*) = 2 \left(\frac{37}{315} - \frac{\Lambda^*}{945} - \frac{\Lambda^{*2}}{9072} \right) \left[2 - \frac{116}{315} \Lambda^* + \left(\frac{2}{945} + \frac{1}{120} \right) \Lambda^{*2} + \frac{2}{9072} \Lambda^{*3} \right]$$

has been tabulated (1).

The equation for $d\theta/dx$ shows that boundary-layer growth can result from viscous causes (first term) or from magnetic causes (second term). If the magnetic term were less than 20 per cent of the viscous term, we could conclude that the standard equations for boundary-layer growth apply reasonably well. Then

$$\frac{\sigma B_{\perp}^2 \theta^2}{\rho \nu} < \frac{F(\Lambda^*)}{20}$$

where $F(\Lambda^*)$ can vary between -0.06 and 1.72 , but for a flat plate, a typical value would be $F(\Lambda^*) \approx 0.2$. That is, magnetic effects are unimportant for boundary-layer growth if $\frac{\sigma B_{\perp}^2 \theta^2}{\nu} < 10^{-2}$. If $\frac{\sigma B_{\perp}^2 \theta^2}{\nu} > 1$, viscous effects are small with respect to magnetic effects. Note, however, that in this case the no-slip boundary condition must be retained.

Two other results of general interest can be inferred from this analysis:

(a) The electric field does not appear in the momentum equation nor in the shape factor Λ^* . Thus, for a given $U(x)$, the boundary-layer behavior is unaffected by the electric field. This can be explained physically by noting that the variations of E in a boundary-layer thickness are assumed to be so small that the same E field acts on the boundary layer as on the free stream adjacent to the boundary layer. The $\sigma(\underline{E} \times \underline{B})$ force in the free stream produces a pressure gradient which, when it is transmitted down into the boundary layer, just balances the $\sigma(\underline{E} \times \underline{B})$ force there. Hence no changes in the velocity profile are produced.

(b) The form of the shape factor

$$\Lambda^* = \frac{\delta^2}{\nu} \frac{dU}{dx} \left[1 + \frac{\sigma B_{\perp}^2}{\rho \frac{dU}{dx}} \right]$$

suggests that a magnetic field can inhibit boundary-layer separation in a conducting fluid. Pohlhausen's analysis predicts separation at $\Lambda^* = -12$. While experiments have shown that this is only approximate, the expression for Λ^* shows that it can be controlled over very wide limits by the magnetic field. If $\frac{\sigma B_{\perp}^2}{\rho \frac{dU}{dx}} = -1$, for instance, $\Lambda^* = 0$ for any Λ ,

and clearly separation is not possible. This criterion should indicate the approximate field strength required for boundary-layer control.

The method of Holstein and Bohlen (1) can be adapted to integrate the von Karman equation for the Pohlhausen profile. If we define

$$z \equiv \frac{\theta^2}{\nu}$$

$$K^* \equiv \frac{\theta^2}{\nu} \left(\frac{dU}{dx} + \frac{\sigma B_{\perp}^2}{\rho} \right) = \Lambda^* \left(\frac{\theta}{\delta} \right)^2$$

then the momentum equation for the Pohlhausen profile becomes

$$\frac{dz}{dx} = \frac{F(\Lambda^*) + 4 \frac{\sigma B_{\perp}^2 z}{\rho}}{U}$$

(II. PLASMA DYNAMICS)

Values for $F(\Lambda^*)$, $\frac{\delta^*}{\theta}$, and $\frac{\tau_o \theta}{\mu U}$ as functions of Λ^* have been tabulated (1).

Integration in closed form is often possible if an approximation of Walz (1) is used: $F(\Lambda^*) \approx 0.470 - 6K^*$. This approximation is good for $K^* > -0.04$, and is excellent for $K^* > 0$.

For instance, we may wish to specify a flat-plate boundary layer for which $\frac{dU}{dx} = 0$ so that $\Lambda^* = \frac{\sigma B_{\perp}^2 \delta^2}{\rho \nu}$, and $K^* = \frac{\sigma B_{\perp}^2 \theta^2}{\rho \nu} = \frac{\sigma B_{\perp}^2 z}{\rho}$. Then,

$$\frac{dz}{dx} = \frac{F\left(\frac{\sigma B_{\perp}^2 z}{\rho}\right) + 4 \frac{\sigma B_{\perp}^2 z}{\rho}}{U}$$

For this flow, the method of Walz is an excellent approximation:

$$\frac{dz}{dx} = \frac{0.470}{U} - 2 \frac{\sigma B_{\perp}^2 z}{\rho U}$$

The solution is

$$\frac{\sigma B_{\perp}^2 z}{\rho} = 0.235 \left(1 - \exp\left(-2 \frac{\sigma B_{\perp}^2 x}{\rho U}\right) \right) \quad (2)$$

The criterion for significant magnetic effects in the boundary layer is that $(\sigma B_{\perp}^2 \theta^2)/\rho \nu > 10^{-2}$. If we use Eq. 2, this becomes $(\sigma B_{\perp}^2 x)/\rho U > 0.02$.

Plans for future work include verification of these results with experimental data if they become available. If there are none, experiments with mercury or NaK will be considered.

D. A. East

References

1. H. Schlichting, Boundary Layer Theory (Pergamon Press, London, 1955), Chapter XII, par. B.